MARTIAN SPECTRAL REFLECTIVITY PROPERTIES FROM MARINER 7 OBSERVATIONS

Thesis by

James Alfred John Cutts

In Partial Fulfillment of the Requirements

for the Degree of

Doctor of Philosophy

California Institute of Technology

Pasadena, California

1971

(Submitted January 19, 1971)

ACKNOWLEDGEMENTS

I wish to thank Dr. Bruce C. Murray for suggesting the Mariner 69 photometric data as material for a research project and for his able guidance in bringing it to completion.

A large part of the analytical work was performed using the facilities of the Image Processing Group at the Jet Propulsion Laboratory. This was made possible through the aid of Mr. Thomas C. Rindfleisch who also advised on the problems of data processing. J.A. Dunne, H.L. Frieden, and W. Stromberg, all of the Jet Propulsion Laboratory, also helped in this respect.

In defining the cartographic methods helpful conversations were had with Dr. R.B. Leighton and Mr. Merton Davies of the Rand Corporation. Discussions with Dr. Conway Leovy of the University of Washington and Dr. L.A. Soderblom of the United States Geological Survey were useful in interpreting the spectral reflectivity observations.

The aid of Mr. Jurrie van der Woude who advised on and participated in the layout of the figures was invaluable.

Finally, a very special acknowledgment is due my wife, Karen, whose encouragement carried me through the most discouraging phases of the work.

Part of the research cost was supported by the National Aeronautics and Space Administration by means of Grant NASA-105-69838.

The work carried out at the Jet Propulsion Laboratory was sponsored by the National Aeronautics and Space Administration under Contract No. NAS 7-100.

ABSTRACT

An analysis of data taken by the Mariner 6 and Mariner 7 spacecraft has been made in order to extend the knowledge of spectral reflectivity differences on the surface of Mars. The data were collected with the Mariner wide-angle television camera which utilizes a vidicon image tube as sensor. The data consist of a series of pictures taken through sequenced color filters with passbands in the visible region of the electromagnetic spectrum (0.43 - 0.65 microns). The Martian regions photographed lie in the longitude range 300° to 30° (East Longitude) and include the prominent dark areas Meridiani Sinus, Sabaeus Sinus, and Margeritifer Sinus, as well as the light 'desert' areas Moab, Thymiamata and Deucalionis Regio.

It was necessary to remove harmonic noise from the television images in order to detect and measure significant spectral reflectivity differences in the equatorial regions of Mars. The resolution element near the center of the planetary disc was 30 km. by 200 km. The measurements represent an order of magnitude improvement in linear spatial resolution over previous measurements made with earth based telescopes and comparable broad band spectral resolution. No reliable published measurements exist for these regions of Mars but the new measurements showed a general agreement with the previous low resolution measurements of other parts of the planet.

The colors of Martian features are very sensitive to the geometry of illumination and viewing. However, color differences attributable to geographic variations in the reflecting properties of the surface and/or atmosphere are recognized in an area near the center of the martian disc. The reflectivity ratio red/green for these areas is strongly correlated with the normal albedo but varies inversely as the reflectivity ratio blue/green. The spectral resolution of the system for measurements within the dark area Meridiani Sinus is limited by aliasing effects with small albedo features.

The dependence of color on local geometry is investigated on the assumption that all the martian features in an area extending from 20°N to 30°S and from 310°E to 30°E have the same correlation between color and normal albedo when this is measured under standard illumination and viewing conditions. Models of a wavelength dependent photometric function and of a uniform atmospheric scattering layer are both consistent with the data.

Atmospheric scattering alone can account for the local geometry effect but if the scattering layer is geographically uniform and independen of Martian local time the atmospheric optical depth is three times that predicted from ultraviolet reflectivity measurements.

Near the center of the martian disc, three distinct reflectivity groups (D, L_1 & L_2) are recognized indicating the existence of abrupt transitions in reflectivity and extensive homogeneous areas with little variation in intrinsic reflectivity. These areas are identified and the boundaries between them studied using high resolution photography. The

boundary between the areas with reflectivities D and L_1 corresponds to a change in surface reflectivity. The boundary between the areas with reflectivities L_1 and L_2 corresponds to the edge of a cloud or haze layer. The reflectance properties of this layer are comparable to those which have been previously measured from limb photographs.

Color-color plots and color-reflectivity plots for Martian surface areas show some similarities with the moon but significant differences. Martian light and dark areas cannot be explained as simply different polymers of carbon suboxide. It may be possible to match the reflectivity characteristics of both light and dark areas with oxidized basalt but if this is the case there must be a change in particle size as well as composition.

TABLE OF CONTENTS

Chapter		Page
I.	INTRODUCTION	1
	a) The Mariner '69 Television pictures	1
	b) Application of the three color data	2
II.	DATA REDUCTION	5
	a) Decalibration of raw data	5
	b) Conversion to Mercator Projection and registration	6
III.	RESULTS - BROAD BAND REFLECTIVITIES OF MARTIAN FEATURES	9
	a) Comparison with ground based measurements	10
	b) Analysis of color ratios of individual resolution elements.	12
IV.	EVIDENCE BEARING ON REFLECTION OF LIGHT FROM THE SURFACE AND ATMOSPHERE OF MARS	14
	a) Surface reflectance and reflectivity boundaries	14
	b) Atmospheric hazes.	15
	c) Atmospheric scattering visible as features	16
V.	EFFECT OF LOCAL GEOMETRY ON MEASURED REFLECTIVITIES	18
	a) Interpretation of increase in blue towards the terminator Models A, B and C	18
	b) Discussion	24
VI.	INTERPRETATION OF THE INTRINSIC REFLECTIVITY AND COLOR OF MARTIAN FEATURES	28
	a) The boundary of Meridiani Sinus	29

TABLE OF CONTENTS (CONT.)

Page

b) The Moab Thymiamata boundary 31

c) Comparison of the color and normal albedo differences on the martian surface with those on the lunar surface 33

d) Significance of color difference between martian light and dark surfaces 35

VII. SUMMARY AND IMPLICATIONS 37

APPENDICES

A. The Nature of the Mariner 7 Digital Television Date and its Decalibration. 70

B. Mercator Projections from Mariner 7 near Far Encounter Images 76

C. Martian Photometry 79

LIST OF REFERENCES 90

LIST OF ILLUSTRATIONS

1. Decalibration - Conversion of Raw Data to Photometric Form 48

2. Shows the Transformation of Photometric Images into Mercator Coordinates. 49

3. The Apparent Color Ratios of Major Martian Features 50

4. The Bivariate Distribution of Color Ratios within Martian Features Shown Using the CLUSTR Program 51

5. The distribution of Color Groups on Mars Shown Using the COLMAP Program 52

6. The Relationship between R/G and B/G and R/G and Go (Normalized Green Reflectivity) for Martian features near the center of the disc 53

LIST OF ILLUSTRATIONS (CONT.)

		Page
7.	Terminator Blue Shift Model A, No Haze, Wavelength Dependent Photometric Function	54
8.	Contrast adjustment factors for Model A	55
9.	a) Model Hazes	56
	b) Dependence of ks on Haze Level	56
10.	Contrast adjustment factors for Models B and C	57
11.	Terminator Blue Shift, Model B, Uniform "white" haze, Wavelength Independent Surface Photometric Function . . .	58
12.	Terminator Blue Shift, Model C, Uniform "Rayleigh" Haze, Wavelength Independent Surface Photometric Function . . .	59
13.	a) Normal Reflectivity of the Surface of Mars between 0.26 and 0.585 microns	60
	b) Normal Reflectivity of the Martian Atmosphere Based on Model C and the Hord and Leovy Models	60
14.	Color and albedo differences between major martian surface features after correcting for the effect of local geometry . .	61
15.	Comparison of crater densities on Meridiani Sinus and Deucalionis Regio	62
16.	Mosaic of Mariner 7 near encounter photographs showing areas with type D, type L_1 and type L_2 reflectivities . . .	63
17.	Mariner 6 frames of the northern boundary of Meridiani Sinus.	64
18.	Pictures of the martian limb 7N1 and 7N7 showing haze layers above Moab and Chryse	65
19.	Mosaic of mercator projections of 7F67 and 7F69 (Photometrically compensated) showing the relationship of the limb traces for 7N1 and 7N7 to bright features in the areas of Moab and Chryse	66
20.	Comparison of the color and normal albedo differences on the martian surface with those on the lunar surface	67

LIST OF ILLUSTRATIONS (CONT.)

Page

21. Comparison of the color and normal albedo differences on the martian surface with those for possible surface materials 68

FIGURES FOR APPENDICES

A1 (a) Digital Video (DV7) Format 84

(b) Transfer Function between Original 8-BIT DV7 and the Six-Bit Data 84

A2 The Removal of Coherent Noise from Photometric Data . . 85

A3 (a) Spectral Transmission of Mariner 7 Color Filters . . . 86

(b) Solar Spectrum and Vidicon Response, Spectral Reflectivity of Light and Dark Areas of Mars (Earth-Based Measurements) 86

B1 Geometry of Images of Mars 87

B2 Formation of Mercator Projections 88

C1 (a) Local Geometry of Illumination and Viewing 89

C1 (b) Orthographic Approximation for Angle of Incidence (i) and Viewing Angle (ε) 89

LIST OF TABLES

Number

1. Geometrical Parameters of Mariner 7 Images 40

2(a). Summary of Broad Band Reflectivities Determined by Mariner 7 41

2(b). Average Green Broad Band Reflectivity and Color Ratios for Selected Martian Features 42

LIST OF TABLES (CONT.)

Page

3. Comparison of Broad Band Reflectivities Determined by Mariner 7 with Ground Based Spectral Reflectivity Measurements 43

4. Terminator Blue Shift, Model A, No Haze, Wavelength Dependent Photometric Function 44

5. Terminator Blue Shift, Model B, Uniform "white" Haze, Wavelength Independent Surface Photometric Function . 45

6. Terminator Blue Shift, Model C, Uniform "Rayleigh" Haze, Wavelength Independent Surface Photometric Function . 46

7. Comparison with Other Measurements of the Optical Depth of the Martian atmosphere. 47

I. INTRODUCTION

The quantitative analysis of reflected and emitted radiation has been the principal tool for studying the surfaces and atmospheres of the planets for many decades. Recent developments in astronomical technology have revived the subject and established the usefulness of measurements of spectral reflectivity in the study of the nature and composition of planetary surfaces. With the launching of spacecraft carrying photometrically calibrated imaging systems to the moon and planets it has become possible to make spectral reflectivity measurements from vantage points other than the earth with vastly greater resolution than previously possible.

a) The Mariner '69 Television pictures

In late July of 1969, the unmanned spacecraft Mariner 6, built and operated by Caltech's Jet Propulsion Laboratory, approached to within 2000 miles of the equatorial regions of the planet Mars. Almost one week later, an identical craft, Mariner 7, also reached Mars, passing above the southern polar cap. The scientific instruments carried by each spacecraft included two television cameras, each with a vidicon sensor.

For two days prior to encounter (closest approach) of Mariner 6, one of its cameras, Camera B, equipped with a narrow angle telephoto lens took Far Encounter (FE) pictures of the planet. In these pictures the planetary image ranged in size from a small disk at the center of the

field upwards until it more than filled the frame. As the spacecraft swept past the planet, Camera A, equipped with a wide angle lens and sequential color filters, was also operated. These Near Encounter (NE) pictures consisted of overlapping A camera frames, each covering an area of about 10^6 sq. km., with higher resolution B camera frames nested within them.

The picture taking sequence for Mariner 7 was broadly similar except that the A camera was also operated late in the far encounter period. Part of the camera data, a low resolution form containing only every seventh element (1, 8, 15, etc.) of a complete frame, was transmitted directly to Earth in real time without intermediate tape recorder storage. The remaining higher resolution data could not be transmitted in real time, were not tape-recorded and were therefore lost. Nevertheless the picture data recovered from these so-called Late Far Encounter (LFE) pictures contain valuable three-color photometric information for large areas of Mars at a resolution greatly superior to that obtainable with earth-based telescopes. The analysis of these data is the principal subject of this thesis.

b) Application of the three-color spectral reflectivity data

The planet Mars with its thin but significant atmosphere, strong coloration, and surface and atmospheric features which change in intensity and form presents a challenging subject for spectral reflectivity analysis. The technique offers the possibility of recognizing different surface lithologies such as Soderblom (1970) has accomplished

for the moon. But the existence of unknown atmospheric effects and the limited high resolution photography of the surface makes the unravelling of color differences a formidable problem.

Mars shows many conspicuous markings corresponding to reflectivity differences. The higher reflectivity or light areas have been described in the past as deserts and the lower reflectivity or dark areas as mare. While there are areas of intermediate reflectivity these occupy a small part of the planet and the light/dark model provides a useful framework for discussing observations of the planet. Yet the nature and origin of these light and dark markings remain one of the most intriguing questions about the planet that is still unanswered, and spectral reflectivity measurements have considerable application to their study.

The late far encounter images of Mars taken in red, green and blue light were used in the following way:

1. To search for different colors in an extensive area covering light and dark features.

2. To make a high resolution map of the colors so identified

3. To evaluate the effect of the geometry of illumination and viewing on the measured reflectivities.

4. To distinguish and study spectral reflectivity variations due to surface reflectivity differences from those resulting from geographic changes in atmospheric scattering density.

The raw data could only be applied to this scientific study after a complex and prolonged reduction process. Techniques were devised to remove coherent

noise from the data before it could be converted to a photometric form. This was followed by the geodesic problem of finding a planetary coordinate system and then registering images. Only then could the scientific analysis of the data take place.

It is important to recognize that it was not anticipated that late far encounter pictures could be acquired until after the launch of the spacecraft Mariner 7. The region of Mars which could be studied and the time period over which observations could be made were severely limited by the spacecraft orbit and the camera design. This is therefore an exploratory study. It does, however, permit some new and interesting conclusions and presents new data analysis techniques. It also illustrates the potentialities and limitations in spectral reflectivity methods when applied to the study of surface history and surface changes on Mars.

II. DATA REDUCTION

a) Decalibration of raw data

A great deal of manipulation of the raw image data returned from the spacecraft was required to convert it to a photometric form. This is described in detail in Appendix A. The processes in the order of applications were:

i. Restoration of missing data bits

ii. Removal of coherent noise

iii. Removal of reseaus

iv. Optical and electronic geometrical correction

v. Removal of residual image

vi. Photometric decalibration

Techniques were developed by the author to handle each of these operations within the framework of the Jet Propulsion Laboratory Image Processing system VICAR*. Although almost every operation had to be specially tailored to handle late far encounter images, the removal of coherent noise presented the most substantial problem. While techniques had been developed by the JPL staff to remove high frequency noise components in high resolution pictures new techniques had to be developed by this author to handle the relatively low frequency noise components in these low resolution pictures. The six operations described above are collectively designated decalibration.

* Video Image Conversion and Retrieval System

b) Conversion to mercator projection and registration

In order to obtain accurate color information and to achieve a precise comparison of color information with other photometric data and with surface features it was necessary to register the images taken through different color filters. Since images were obtained approximately 88 seconds apart the rotating planet showed a slightly different aspect in each. It was decided therefore to transform the images into the Mercator projection. Such a projection, with latitude and longitude lines forming a net of rectangles, is ideally suited to the algorithms used in a computer generated geometrical projection.

In order to perform this type of Mercator projection it is necessary to accurately locate the intersection of latitude and longitude lines in the frame. Since the measurement of the pointing angle of the cameras is so coarse this information is not available from the spacecraft telemetry data. Davies (1971) has described a system of using craters visible in far and near encounter frames as control points for establishing the latitude longitude net for the planet. Such a system unfortunately is not applicable to the color images because craters are not recognizable in the low resolution late-far-encounter images. Leighton, R.B. (private communication) has devised a technique for establishing these coordinates by measurements on the image of the planetary limb. Only the terminator is visible in the

LFE pictures and consequently this method is not appropriate either.*

A method was developed using small well defined albedo features visible in LFE, FE and NE pictures. The latitude and longitude of the feature was measured in the near encounter picture using the Davies control net referred to above. The position of any latitude longitude intersection in the LFE picture could then be calculated (Appendix B)since the projected tilt of the planet's axis relative to the camera scan lines and the planetary diameter were known (Table 1).

A mercator projection of the region of the planet from +40°E to -50°W longitude and from +20°N to -40°S latitude was formed (Appendix B, Fig. B2) for images taken through the RED, GREEN 1, BLUE and GREEN 2 filters. The accuracy of these projections was refined using a mercator projection of the same region in a far encounter picture 7F67. The latter projection was based on the more accurate cartographic data obtained from the Mariner 69 control network (Davies and Berg, 1971). Each LFE picture was linearly displaced for optimum registration with the albedo features in 7F67. Since these linear shifts were less than 30 KM, then the second order errors involved in the linear shift were negligible in comparison with the intrinsic errors in positioning and it was not necessary to repeat the mercator projection. The accuracy of registration was verified by

* Only the limb of a planet is a useful control point. A dense haze extending to 20 km above the planetary surface can cause only a 20 km error in the location of the limb but up to 200 km error in the location of the terminator.

forming difference pictures with 7F67 (Fig. 2).

III. BROAD BAND REFLECTIVITIES OF MARTIAN SURFACE FEATURES

The methods of the above section permit the rapid calculation of wide band reflectivities (see Appendix A) for accurately located positions on Mars in four wavelength bands. Wide band reflectivities for several classical features shown in Fig. 3 are listed in Table 2(a). The light reflected from the planet includes components from the atmosphere and the surface. Many changes in reflectivity attributable to physical changes on the surface or in the atmosphere have been reported by astronomical observers but the reflectivity also critically depends on the conditions of illumination and viewing. Solar incidence angle, viewing angle and phase angle are therefore given for each area sampled.

In Table 3, the broad band reflectivities are used to calculate an average green reflectivity $G=(G_1+G_2)/2$ and also to calculate reflectivity ratios R/G and B/G described henceforth as color ratios. They are called color ratios because of the analogy with the color vision of the human eye brain system. Two color ratios, for appropriately chosen filter passbands, are adequate to characterize any visible hue.* The color ratios for the features shown in Fig. 3a are displayed in graphical form in Fig. 3.b.

The Mariner data indicate that both light and dark areas on the planet are red in the sense that the reflectivity measured through the

* For precise color reconstruction the Mariner 7 filter passbands do not span a great enough wavelength range.

red filter (R) is greater than that measured through either green or blue filters (R and G). They also indicate that a light feature such as Moab (9) is redder than a dark feature such as Meridiani Sinus (5) in the sense that the value of R/G is greater (Fig. 3(b)).

a) Comparison with ground based observations

It has long been known that the light areas on Mars are red but it is only recently that planetary astronomers have firmly established that the dark areas are red also but less red than the light areas. (Dollfus, 1965) Most measurements of the spectral reflectivity of Mars have been broad band measurements like the Mariner 7 data but unfortunately not in identical wavelength bands. The only ground based data suitable for a comparison are those of high spectral resolution such as those of McCord (1969) which can be used in the relationship given in Appendix A.

$$\text{Broad Band reflectivity} = \frac{\int V_\lambda F_\lambda S_\lambda R_\lambda d_\lambda}{\int V_\lambda F_\lambda S_\lambda d_\lambda} \qquad (1)$$

In Table 3 (b) broad band reflectivities and color ratios computed for the features Arabia and Syrtis Major using this equation with the absolute spectral reflectivities given by McCord (1969) are listed. These features do not appear in Fig. 3 but their reflectivities under similar illumination and viewing conditions are comparable to those of the features Moab (9) and Meridiani Sinus (5) respectively. This assessment is based on a comparison of the features as they appear in the photometrically corrected mercator photomap of Mars (Cutts et al 1971)(b).

Neither broad band reflectivities R, G_1, B, G_2 nor the simple color ratios R/G, B/G as computed for the Mariner data agree with the predicted values based on McCord's ground based measurement. Since different features are being measured under different illumination and viewing conditions and the reflectivity of many Martian surface features is known to vary diurnally and seasonally this is no reason why either should be wrong. However systematic errors do enter into the Mariner determinations as a result of drift in camera sensitivity away from its calibration value(Appendix A). Less sensitive to the drift are the relative quantities such as the ratios of the broad band reflectivities of a light to a dark feature or the relative color ratio computed in Table 4. Certainly there is better agreement between the Mariner data and McCord's data for these quantities.

The superior accuracy of relative reflectivity and relative color ratio measurements is not peculiar to the Mariner camera. McCord (1968) and Soderblom (1970) have expressed their extensive earth-based measurement of the spectral reflectivities of lunar features in relative form using an area in Mare Serenitatis as a reference because of the uncertainty in the transmission of the earth's atmosphere. There might be a case for expressing the data for Mariner features in relative form but unfortunately there is no feature on Mars whose reflectivity is known to be stable and therefore could be used as a standard. Consequently, broad band reflectivities and color ratios are not expressed relative to a

standard feature in this work but it is emphasized that reflectivities and color ratios are more accurate relative to one another than absolutely.

b) Analysis of color ratios of individual resolution elements

To display the total spread of the color ratios in the region of Mars studied here the color ratios R/G and B/G are computed separately for each resolution element and the resulting 8000 values expressed in the form of a histogram (Fig. 4) by means of the program CLUSTR. CLUSTR operates on the digital arrays R/G and B/G from which the color ratio pictures of Fig. 2 (line 4) were derived. The histograms are also computed for smaller features of fairly homogeneous reflectivity (Fig. 2) - the dark feature Meridiani Sinus, the "halftone", i.e. region of intermediate reflectivity Deucalonis Regio and the brightest area Moab. Even these fairly homogeneous features show a distribution of color across their surface which is most conspicuous in Meridiani Sinus. Part of this variation may be contributed by noise and misregistration of small albedo features but there are real color differences in the apparently homogeneous features as is illustrated by the application of the program COLMAP.

Like CLUSTR, COLMAP operates on the digital arrays R/G and B/G shown pictorially in Fig. 3. COLMAP performs the inverse problem, that is, tracing those areas on the planet which contribute to particular parts of the histograms (Fig. 4). A resolution element is assigned a number

and hence a gray level on the basis of which of nine color groups it belongs to. The color ratios R_1, R_2 and B_1, B_2 which define the nine color groupings can be suitably chosen by referring to histograms such as those of Fig. 4. For instance, from Figs. 4(c) and 4(d) it can be inferred that most parts of Moab have R/G 1.33 and B/G .26 whereas most parts of Deucalionis Regio lie on the other side of these values. The display of COLMAP (Fig.5(a)) confirms this but also displays the anomalous areas and the transitions between colors. A similar separation for areas in Meridiani Sinus is shown in Fig. 5 (b).

The most striking aspect of the COLMAP displays (Fig. 5(b)) however, is the increase in blue reflectivity relative to R and G towards the terminator (west). Explanations for this and other aspects of the color of the surface features are discussed in Section V.

IV. EVIDENCE BEARING ON REFLECTION OF LIGHT FROM THE SURFACE AND ATMOSPHERE OF MARS

The light reflected from Mars and recorded quantitively by the Mariner 7 television cameras arises from scattering both in the atmosphere and from the surface of that planet. There is no way that the measurements presented in the last section can be used independently of other data to distinguish atmospheric and surface contributions. It is possible, however, to use information in other data taken by the television cameras and by other experiments on the Mariner 6 and 7 spacecraft to better delineate surface and atmospheric contributions.

a) Surface reflectance and reflectivity boundaries

Many astronomers (Slipher 1962, p. 9) have concluded that the major markings in the equatorial regions of Mars are fixed and represent differences in surface reflectivity and not atmospheric phenomena. This belief is based on the observed permanence of these features during a century of observation. When in 1965, Mariner 4 photographed the planet, a cratered surface was clearly visible through the atmosphere although the surface did appear to be shrouded in a general haze. (Leighton et al 1965). Then in 1969, Mariner 6 and 7 performed a more extensive photographic exploration and it was firmly established that the boundary of one major equatorial feature Meridiani Sinus/Sabeaus Sinus, the dark pipe shaped area, appearing in the region of color coverage (Fig.3), corresponded to differences in surface reflectivity (Cutts, et al 1971).

The new evidence included the diversity of boundary types, unchanging crater densities across certain of these boundaries and the control of topography over the over the configuration of local albedo markings. This boundary at least cannot be the edge of a cloud or haze layer nor can it correspond to a discontinuity in the density of one.

b) Atmospheric hazes

There are two ways of identifying Martian atmospheric scattering in visible light images such as those obtained by the Mariner 7 cameras. Where the scattering layers are optically thick they can be identified in full disc images by means of photometric behavior, diurnal variation, or as actual albedo features. Where the scattering layers are optically thin in visible light they can only be recognized in images of the limb. However, in ultra-violet light the same scattering layers may be optically denser and detectable in oblique or even normal viewing.

Hord and Barth (1971) have interpreted the scans made by an ultra-violet spectrometer (UVS) carried on both the Mariner 6 and 7 spacecraft. They show that scattering of ultraviolet light from the Martian atmosphere seems to depend only on atmospheric pressure in a broad region paralleling the near-encounter coverage of the Mariner '69 television cameras. Yet, this scattering is three times that expected from a pure atmosphere and they infer the presence of a fine particulate suspension, scattering light according to the Rayleigh law, whose optical depth depends only on atmospheric pressure.

Leovy et al (1971) have discussed the detached limb hazes visible

in both near and far encounter television (TVS) pictures. They find that the height and possibly the optical depth of these scattering layers vary laterally across the planet. Non-Rayleigh scattering is inferred from the measured wavelength dependence and optical thickness. Such different characteristics suggest that the scattering measured by the TVS has a different origin than that measured by the UVS. There is however an apparent contradiction. Whereas the haze characterized by the UVS would be invisible in the wavelength band registered by the TVS, the converse is not true. The haze brightness implied by the TVS limb pictures should have resulted in substantially higher UVS reflectance values at .38 micron.

An explanation for these apparent contradictions may be that these investigators have used over simplified models. The qualitative results of the infrared spectra obtained by Mariner 6 and 7 (Herr et al 1969) indicating solid carbon dioxide suspensions near the limb and silicate dust suspension near the terminator demonstrate that the Martian atmosphere contains a variety of suspended particles which have different number densities and height variations. Furthermore the conclusions of Leovy et al (1971) are dependent on assumptions about the photometric characteristics of the martian surface.

c) Atmospheric scattering visible as features

The thin hazes indicated by these TVS and UVS measurements would only contribute a fraction of the reflectivity of the planet and therefore would not be easily visible as features against the disc. Yet there

are well defined albedo markings visible, which may be the manifestation of atmospheric phenomena, and if so must have much greater optical depths in the wavelength band of the TVS than those discussed above. The small scale markings visible in the region of Nix Olympica (20°N, 135°W) could be atmospheric in origin (Leovy *et al* 1971). The area over the north polar regions of the planet which appears so bright in the blue image (Fig. 2) may also be atmospheric since it shows no craters along its diffuse boundary and differs in color from the surface deposits of the south polar cap. Neither can one completely discount the possibility that the vast Hellas basin owes its high reflectivity to a dense haze obscuring a cratered surface. Indeed, until demonstrated otherwise atmospheric effects must be considered as a possible explanation of the reflectivity variations observed over the entire planet.

V. EFFECT OF LOCAL GEOMETRY ON MEASURED REFLECTIVITIES

a) Interpretation of the increase in blue towards the terminator

A striking feature of the color maps (Fig. 5a and 5b) pointed out in section III is the substantial increase in blue reflectivity relative to other colors in the region nearest the terminator. This effect has been recognized in earth based telescope photographs to take place both near the bright limb and also near the dark limb (terminator) of the planet. It could result from diurnal variation in the reflectivity of the surface (frost) or a change in the optical density of the atmosphere (cloud condensations). However, even if there were no such diurnal changes the effect could still be explained in terms of the change in the geometry of illumination and viewing (local geometry).

There are two ways in which changes in local geometry can change the apparent color of the martian features. In the first place they alter the relative contribution of surface and atmospheric light to the measured brightness. Approaching the terminator the proportion of atmospheric light increases and if the atmosphere is bluer than the surface the total light reflected from the planet will become bluer. A second effect, not dependent on the existence of a significant scattering atmosphere, is wavelength dependence of the surface photometric function. Aggregates of fine particles, such as those that are believed to form the martian surface may exhibit this phenomen.

In a small region near the center of the martian disc (Fig. 6) changes in local geometry are small and the changes in reflectivity and color that occur are almost entirely due to physical changes in the surface

and possibly also in the optical depth of the atmosphere. The relationship between the color ratio R/G and the normalized green reflectivity (Go)[1], (Fig. 6) is of particular interest. The histogram shows two major groups: the dark areas (Go= .087 to .095) and the light areas (Go= .110 to .125), and indicates why it is possible to make such a clear distinction between martian areas on the basis of reflectivity. The subdivision of light areas in this region into two groups is discussed later in the text.

Whereas the histogram shows no other maxima it does show a conspicuous minimum (Go= .102, R/G= 1.24). This results from residual misregistration of the red, green and blue images used to form the color ratios. Those color ratios in the histogram which surround the minimum are artifacts. The fine corrections necessary to remove these artifacts are incorporated in the histogram of Fig. 14, which then shows a strong correlation of Go with R/G. This strong correlation indicates that the same factors which cause the reflectivity differences on the planet are responsible for the color differences.

If the strong correlation between intrinsic color and reflectivity that exists in the area within the small rectangle of Fig. 6 also applies to the entire region then it is possible to further investigate the terminator blue shift. In the analysis below it is assumed that the relative color ratio red/blue for the martian surface is proportional to the green reflectivity. for normal illumination and viewing. The consequences of this assumption

[1]Computed from the Minnaert law (Appendix C) assuming k=0.6

are worked out below for three models of the surface and atmosphere of Mars.

Model A

On this model scattering of light by the atmosphere is taken to be negligible and the color change towards the terminator is attributed to a wavelength dependent photometric function. The reflectivity of the Martian surface is taken to obey the Minnaert photometric law (Appendix C., Eq. 3)

$$\text{Surface Reflectivity } \mathcal{R}_s = \mathcal{R}_{os}(\alpha,\lambda) \cos i^{k_s(\alpha,\lambda)} \cos \epsilon^{k_s(\alpha,\lambda)-1}$$

Since only measurements at a single phase angle are discussed here (and in Models B and C) this equation simplifies to

$$\mathcal{R}_s = \mathcal{R}_{os(\lambda)} \cos i^{k_s(\lambda)} \cos \epsilon^{k_s(\lambda)-1} \qquad (1)$$

The functional form of $k_{s(\lambda)}$ is taken to be

$$k_s(\lambda) = k_{sG} + C_1 (\lambda - \lambda_G) \qquad (2)$$

where k_{sG} = Minnaert parameter for green average (G)

λ_G = effective wavelength for green average (G)

C_1 = constant to be evaluated

λ = effective wavelength of filter (red or blue)

$k_s(\lambda)$ = Minnaert parameter at effective wavelength λ

Normalised reflectivities $\mathcal{R}_{os}$ were calculated for the red (R), green average (G) and blue (B) mercator photometric data for each resolution element using formulas (1) and (2) and the techniques of Appendix C for four values of C_1: 0, 5/6, 10/6 and 15/6. The following notation

is used for these normalised reflectivities.

$$R_{os} = \mathcal{R}_{os} \quad \text{(RED)} \tag{3}$$

$$G_{os} = \mathcal{R}_{os} \quad \text{(GREEN)} \tag{4}$$

$$B_{os} = \mathcal{R}_{os} \quad \text{(BLUE)} \tag{5}$$

The color ratio R_{os}/B_{os} is displayed in pictorial form for each value of C_1 in column 1, Fig. 7 and the value of k_s for each color is shown for each image.

In Fig. 8 and Table 5 the average values of R_{os}/B_{os} and G_{os} are shown for both a light (high reflectivity) and a dark (low reflectivity) feature near the center of the Martian disc. These values define a linear relationship

$$G_{os} = D_1 + D_2 \, (R_{os}/B_{os}) \tag{6}$$

for each value of C_1 and simultaneous equations can then be written to solve for the constants D_1 and D_2. It is assumed that this same linear relationship holds for all features in this region of the planet and to test this assumption the value of the normal green reflectivity is predicted from the color ratio

$$G_{os}{}^{1} = (R_{os}/B_{os})^{1} = D_1 + D_2 \, (R_{os}/B_{os}) \tag{7}$$

In Column 2 of Fig. 7, $G_{os} = (R_{os}/B_{os})^{1}$ is ratioed with G_{os} and displayed pictorially. If a linear relationship did hold between color and reflectivity for the region, then this picture would be quite flat and without any gross changes in intensity. Contouring of the intensity levels in this ratio picture (column 3) shows that a photometric color factor $C_1 = 15/6$ comes closest to realizing this objective.

It corresponds to $k_s = 0.45$ for the blue, 0.6 for the green and 0.75 for the red filter.

Model B

Model B assumes that the photometric function of the Martian surface is independent of wavelength and that the color change towards the terminator is attributable to atmospheric scattering. An optically thin 'white' or neutral haze (Appendix C) is assumed, these characteristics being those inferred by Leovy et al (1971) for the thin hazes visible in Mariner 7 near encounter limb photographs and discussed in Section IV.

A method of analysis similar to that applied to Model A is adopted here but instead of a parameter in a wavelength dependent photometric function it is now a haze level which must be fitted to the data. The normal reflectivity of each haze tested is shown in Fig. 9(a). The reflectivity of the atmospheric scattering layer ($\mathcal{R}$ a) is calculated for each filter passband and for each resolution element in the region shown in Fig. 3 using equations (5) and (8) of Appendix C. This is subtracted from the total reflectivity ($\mathcal{R}$ t) of the planet and the residual is taken to be light reflected from the surface ($\mathcal{R}$ s).

Evaluation of the color ratio (R_{os}/B_{os}) is much simpler than for Model A because the photometric function of the surface of Mars is assumed to be independent of wavelength.

$$(R_{os}/B_{os}) = (R_s/B_s) = \mathcal{R}_s \text{ (RED)} / \mathcal{R}_s \text{ (BLUE)} \qquad (8)$$

However, evaluation of the normalised green reflectivity (G_{os}), is much more complicated since the value of k_s, the Minnaert constant for the planetary

surface, is dependent on the haze parameters.

In Model A, there was assumed to be no atmospheric scattering and k_s was equal to the observational value of k.[1] The relationship between k_s and this observational k ($=k_t$) when there is significant atmospheric scattering is shown in Fig. 9(b). It is a function of the photometric coordinates because the simple Minnaert law cannot represent the total scattering from surface and atmosphere even when considered independently these are Minnaert scatterers. Since no photometric analysis has been performed for this part of Mars and no suitable data exist it is not possible to define k_s uniquely. The value of k_s for sec $\epsilon = 1.2$ was taken to be representative of the region.

Following the method used for model A the proportionality constants D_1 and D_2 were determined from light and dark areas near the center of the martian disc (Table 6 and Fig. 10(a)). These constants differ from those of Model A and vary significantly with the value of H, the haze reflectivity. $(R_{os}/B_{os})^1$ is calculated for the entire region as before and ratioed with G_{os} (column 2, Fig. 11). Contouring of this ratio (column 3, Fig. 11) is the final operation which determines whether a haze value provides a good fit to the data.

Model C

This is almost identical to Model B. The analysis is identical but a 'blue' Rayleigh scattering haze (Appendix C) rather than a 'white' haze is used. The haze levels used are shown in Fig. 8(a). The proportionality factors D_1 and D_2 are recorded in Table 7 and displayed in

[1] The observational value applies to the total light reflected by the planet

Fig. 10(b). The attempts to match the data with three different Rayleigh haze levels are shown in Fig. 12.

b) Discussion

In a small region near the center of the martian disc the changes in local geometry cannot significantly affect the measured reflectivities and colors. In this region there exists an almost linear relationship between normal reflectivity and color. Other martian features nearer the terminator of the planet display different spectral properties. A test has been made of whether these differences can be accounted for merely by the change in local geometry. To make this test, models based on observation of the planet and on laboratory experiments were employed to restrict the number of free parameters of the problem.

Of the three models considered Models A and C provide an acceptable match to the data. It is not possible to match the data with Model B since haze reflectivities large enough to account for the gross trend in color towards the terminator exceed the total measured reflectivity in illuminated parts of the planet near the terminator. In optimizing Models A and C we obtain solution for either the photometric function or for the optical depth of the Martian atmosphere. These solutions are now evaluated in terms of other observational data.

It is difficult to find a physical basis for the extreme wavelength dependence in the photometric function which is implied by Model A. Darker materials do have a lower value of k (Young and Collins 1971) and since the reflectivity of the martian surface is lower at shorter wavelengths this could be

a partial explanation but no quantitative data on this effect are available. The lunar surface for which a substantial amount of photometric data is available shows no comparable effect. The color of lunar features has only a barely detectable phase angle dependence. Furthermore, in the study of lunar colors at constant phase angle but with illumination and viewing angles varying (Soderblom 1970) none of the color differences have been attributed to the photometric function. There is clearly a need for more data on this phenomenon.

Model C is of much greater interest because here it is possible to make direct comparisons with other observations. In Table 7, Models B and C are compared with other models of the optical characteristics of the Martian atmosphere. The parameters tabulated for Model C are optimal for the entire region between 20°N and 30°S; those tabulated for Model B provide a moderate fit for a narrow (10° to 20°) strip lying along the equator. The most interesting and relevant comparisons are with the models of Leovy et al (1971) based on Mariner 7 photographs of detached limb hazes and that of Hord and Barth (1970) based on scans of the ultraviolet spectrometer on the Mariner spacecraft. These models have already been discussed in Section IV and are both based on measurements made within three hours of the time that the Mariner 7 near-far-encounter (LFE) images were acquired.

The Hord model is most directly comparable with Models B and C since it applies to the entire depth of the atmosphere right down to the surface. According to this model, scattering in the atmosphere of Mars has a Rayleigh wavelength dependence (Appendix C) but is three times that expected from the pure atmosphere and the Rayleigh phase function is also assumed to apply. At

the shortest ultraviolet wavelength (.26 microns) surface reflectivity is taken to be negligible but at the longer wavelengths up to .36 microns it is determined as the difference factor necessary for exact Rayleigh wavelength dependence.

In Fig. 13, the optical characteristics of the surface and atmosphere of Mars at zero phase and viewing angles are shown for the Hord model and for Model C. These characteristics were calculated using the photometric functions given in Appendix C. The values of Martian surface reflectivity ($\mathcal{R}_{os}$) which are obtained are not inconsistent with one another and the dashed line (Fig. 13a) indicates a smooth interpolation between the wavelength range of the UVS and the television system. However, the values of normal atmospheric reflectivity ($\mathcal{R}_{oa}$) which are derived from the models do not agree satisfactorily with one another. If atmospheric scattering has a Rayleigh wavelength dependence between .26 and .36 micron then it should be possible to extrapolate to the longer wavelengths of visible light (Fig. 13b). Yet this gives a value of $\mathcal{R}_{oa}$ at .525 microns only one quarter of that inferred from Model C.

The Leovy models (Leovy et al, 1971) apply strictly to hazes detached from the surface of the planet and visible in a linear zone near 25°N and extending from 350°E to 20°E. Detached hazes have also been identified in the lower resolution far encounter frames and although no quantitative measurements have been made from these frames it has been demonstrated that the detached haze layers are patchy and not uniformly distributed around the planet (Leovy et al 1971). Unfortunately, the detached hazes in the vicinity of Meridiani Sinus have not been identified in far encounter photographs and there is no means of judging whether or not they are uniform over the region

on which Model C is based.

In Fig. 13 the normal atmospheric reflectivities ($\mathcal{R}_{oa}$) calculated from Leovy's Models 1 and 2 for the detached haze[1] are compared with those calculated from Model C and the Hord model. The values of $\mathcal{R}_{oa}$ for the Leovy models lie very close to those for Model C throughout the visible spectrum. At .525 microns $\mathcal{R}_{oa}$ for Model C is bracketed by the values of $\mathcal{R}_{oa}$ for Models 1 and 2. However, the wavelength dependence and implicitly the phase angle dependence of the scattering in the Model C atmosphere are not compatible with Models 1 and 2.

The general agreement of the calculated atmospheric characteristics with the independent determinations demonstrates that the color of a surface feature is very sensitive to the local geometry of illumination and viewing. Therefore in this particular study since there is inadequate knowledge of the nature and magnitude of the local geometry effect, intrinsic color variations can only be studied in a limited area near the center of the disc.

[1] Models 1 and 2 are different interpretations of the same basic data

VI. INTERPRETATION OF THE INTRINSIC REFLECTIVITY AND COLOR OF MARTIAN FEATURES

In the region near the center of the martian disc encompassing parts of Meridiani Sinus, Moab, Sabaeus Sinus and Deucalionis Regio (Fig. 6) color and albedo differences are primarily accounted for by geographic changes in the reflecting properties of the surface and/or atmosphere. The effect of local geometry is negligible as is demonstrated in Fig. 21. The presence of a uniform scattering haze such as that proposed in Model C does not significantly alter the relative values of color and albedo (normal reflectivity) for the martian light and dark markings.

COLOR-COLOR histograms of the area identified in Fig. 6 only show two basic maxima. The one due to the dark areas is broader and this characteristic is due to residual misregistration of the small albedo features. In Fig. 14 the program COLMAP is used to identify the colors of surface features. The dark areas are clearly identified as the blue features and Moab is identified as the reddest feature but no other well defined groupings can be identified.

The relationship between color and albedo (Go) shown in Fig. 6 is more interesting. Three distinct maxima appear in the histogram. The first is labelled D and corresponds to the dark marking Meridiani Sinus (Fig. 14e). L_1 and L_2 which are much closer in color and albedo to one another than either is to D are both classical desert areas. L_2 which corresponds principally to the area Moab is the highest reflectivity area (Fig. 14c).

In order to interpret the nature of the martian regions that correspond to these three maxima it is necessary to study physical boundaries between them on the planet. The best example of the boundary between type D and type L_1 areas is the boundary of Meridiani Sinus. The L_1 and L_2 regions adjoin at the reflectivity boundary near 10°E longitude (Fig. 14e) which extends irregularly from the martian equator to 20°N and beyond. This is considered here as synonymous with the boundary between the classical features Moab and Thymiamata. The high resolution photography of this region of the planet which was obtained by Mariners 6 and 7 is incorporated in the interpretations.

a) The boundary of Meridiani Sinus

Reflectivity types L_1 and D meet at the boundary of Meridiani Sinus and high resolution photography shows the width of the transition zone to be larger along the northern and western parts of the boundary than in the southern and eastern parts (Cutts et al 1971 a). The Late Far Encounter photometric data were not of sufficiently high resolution to show this effect and the width of the transition zone indicated in the registration test (Figs. 14b & d) is strongly affected by aliasing effects (See Caption, Fig. 14). The high resolution photographic data are now used to demonstrate that this boundary corresponds to a change in surface reflectivity and that it is not the edge of a cloud or a discontinuity in an atmospheric haze layer.

Across the southern boundary of Meridiani Sinus there is no apparent change in crater density (Figs. 14e & f). This is confirmed by the comparison of crater abundances in Meridiani Sinus and Deucalionis Regio (Fig. 15).

If this boundary corresponded to the edge of a cloud or a discontinuity in an atmospheric reflecting layer then the visibility of craters would change across it. Since there is no significant change in crater density this suggests that the boundary corresponds to a change in surface reflectivity.

A much stronger argument can be made in terms of craters which are associated with albedo markings. Craters displaying light markings either on floors and/or walls are widespread in Meridiani Sinus (Fig. 16). These light markings are usually confined to the northern parts of the crater floors and to south facing slopes. The reflectivity variations cannot be attributed to insolation variations (the sun is north of zenith in Fig. 16) nor can one establish a plausible explanation involving variations in photometric function.

The extent of these albedo markings in large flat-bottomed craters changes gradually across an albedo boundary. This is displayed in frames 6N11 and 6N13 (Fig. 17). In crossing the diffuse boundary from Meridiani Sinus to light Thymiamata (6N11) the light markings become more extensive covering greater portions of the walls and floors of the crater. Farther into the light area only a small dark patch on the southern part of the floor remains; still farther dark markings disappear altogether. These relationships suggest the possibility that the light materials surrounding craters in the light region and occurring inside craters in both light and dark regions are of the same nature and origin.

If the materials responsible for these light markings were suspended in the atmosphere it seems very unlikely that their distribution could be controlled by the low relief of the martian craters. It is concluded that the materials

inside the craters are on the surface and that the boundary of the dark feature Meridiani Sinus involves a change in surface reflectivity of essentially the same nature.

b) The Moab Thymiamata boundary

Reflectivity types L_1 and L_2 are found over the desert areas of the planet which are the non polar high reflectivity areas adjoining the fixed dark markings like Meridiani Sinus. The two groups L_1 and L_2 are best defined with respect to the reflectivity boundary near 10°E longitude which extends irregularly from the martian equator to 20°N. The area to the west of the boundary corresponding to the classical feature Thymiamata belongs predominantly to the L_1 subgroup. The area to the east of the boundary which can be identified with the classical feature Moab is predominantly in the L_2 subgroup. The boundary itself corresponds in location to two of the many dark lines found in early maps of Mars and identified as the "canals" Gehon and Hiddekel. These lines are clearly spurious (Cutts et al 1971 a) but the important question now is whether the boundary represents the edge of a cloud or a change in surface reflectivity. The photographic and photometric evidence bearing on this question are now assessed.

The interpretation of the boundary of Meridiani Sinus in terms of a change in surface reflected required the use of high quality, near vertical photographic coverage. The photography of the Moab/Thymiamata boundary is oblique (Fig. 16) with near vertical illumination and no topographic features can be resolved within the area of Moab. Different methods must therefore be used in studying this boundary.

A television image of the martian limb (picture 7N7) suggests that the Moab/Thymiamata boundary corresponds to a change in the density of atmospheric haze. Photometric versions of this picture and also of 7N1 reveal increases in haze density both to the east and to the west of zero longitude. Over the region Thymiamata near zero longitude, the haze density is very much lower (Fig. 18).

In Fig. 19, the traces of the limb in 7N1 and 7N7 are superimposed on to a section of the Mercator photomap of Mars (Cutts et al 1971b) which is derived from Mariner 6 and 7 far encounter pictures. The areas of greatest haze density correspond to bright markings in the region of Chryse (20°N, 30°E) and to the high reflectivity area Moab. This evidence strongly suggests that the Moab/Thymiamata boundary between the L_1 and L_2 spectral types corresponds to the margin of an extensive atmospheric haze layer.

The photometric data on L_1 and L_2 can be used to study the color and optical density of this layer. Since the limb photograph (7N7) shows the haze layer to be detached it is optically thin and the total reflectivity of the Moab region is the sum of the reflectivity of the surface and of the haze layer (Appendix C, equation 9).

The reflectivity of the haze layer can therefore be calculated as the difference in reflectivities on each side of the Moab/Thymiamata boundary.

In Fig. 13(b), the optical properties of the haze layer over Chryse computed by Leovy et al (1971) from photometric limb profiles on 7N1, 7N2, 7N3 and 7N5 are compared with the optical properties of the Moab haze layer (Model Y). The determinations are made from significantly different phase angles and in order to make the comparison the Rayleigh phase function is assumed. The

Moab haze layer seems significantly redder than the Chryse haze layer and somewhat less dense. However, the comparison is very sensitive to the exact form of the phase function.

c) Comparison of the color and normal albedo differences on the martian surface with those on the lunar surface

It was demonstrated in Section VIa that there are significant variations in color and normal albedo on Mars which are attributable to geographic variations in surface materials. Such differences have also been recognized on the moon and have been studied remotely by means of earth-based telescopes and also directly using samples recovered from the Apollo missions. Chemical and petrological studies of the lunar rocks have also been made therefore a comparison of the spectral reflectivity properties of the lunar and martian surfaces is particularly instructive.

Martian color variation is compared with lunar color variation in the relative COLOR-COLOR plots of Fig. 20. The lunar measurements were taken over a broader spectral range but for the purpose of this comparison the lunar and martian measurements were normalized to a spectral separation of .1 microns. Although the range of lunar colors is much smaller a similar kind of variation exists as for Mars with the increase in RED/GREEN color accompanied by a decrease in BLUE/GREEN color indicating a minute rotation of the spectral curve in the visible region.

Soderblom (1970) has recognized areas of homogeneous color in the lunar maria which he associates with distinct episodes of vulcanism (Fig. 20). The spectral resolution required to resolve comparable regions within the martian dark areas, for example, is far beyond the capabilities of the Mariner camera

system.

The COLOR-REFLECTIVITY histogram for the lunar surface (Fig. 20) shows significant differences from that for the surface of Mars. Whereas the range of colors is much greater for Mars the range of reflectivities is much greater for the moon. Within the lunar maria the range of reflectivities is very small and the RED/GREEN value increases with reflectivity just as it does for Mars. However, the upland areas which show a very large range in reflectivity are all essentially the same color as the maria.

There is still no general agreement as to why the lunar maria and uplands are so similar in color and yet so different in reflectivity. Study of the lunar rocks recovered from the lunar maria by Apollos 11 and 12 and in-situ experiments performed by the unmanned Surveyor spacecraft have provided new insight into the problem. One possibility is that in the lunar uplands there is a much smaller proportion of the dark glasses which occur in the lunar maria as individual beads and coating small particles. Another possibility is that there is a greater abundance of very fine particles (ten to one hundred microns diameter) on the lunar uplands. In certain silicate materials changing particle size can substantially effect the reflectivity of a surface without changing its color. It is not unlikely that both these effects contribute to the reflectivity difference between lunar uplands and maria. The close correlation between the color and the normal reflectivity of martian surface features suggests a common origin. The nature of this correlation is similar to that observed for the lunar maria but the total range in color and reflectivity is much larger. In the absence of reliable data on the origin of lunar color and albedo variations the nature of these differences on the martian surface

can best be studied in terms of laboratory measurements.

d) Significance of color difference between martian light and dark surfaces

In Fig. 21 the COLOR-COLOR and COLOR-REFLECTIVITY plots for Mars are compared with plots based on laboratory data to illustrate the requirements placed on possible martian surface materials. Both carbon suboxide (C_3O_2) and oxidized basalt have recently been suggested as the martian surface material (Plummer and Carson 1969, Adams and McCord 1969). Both materials provide close fits to the spectral curves for light areas of the planet in both the visible range and the infrared part of the spectrum. They are the only materials which seem geologically or meteorologically reasonable which are known to show such close agreement. It is a valid exercise therefore to investigate if the spectral differences between light and dark areas of Mars can be explained in terms of alteration of these materials.

Carbon suboxide becomes redder with increasing polymerisation and the plot of RED/GREEN ratio against BLUE/GREEN ratio for these polymers (Fig. 21) is not inconsistent with the martian data. However, when carbon suboxide gets redder it also gets darker and the incompatibility of this characteristic with the martian data is shown in the COLOR-REFLECTIVITY plot of Fig. 21. Basalt also undergoes a color change when the proportion of ferric iron (Fe^{+++}) is increased by either the addition of goethite or oxidation with nitric acid. Again the COLOR-COLOR plot is compatible with the difference between martian light and dark areas but the COLOR-REFLECTIVITY plot is not. It is concluded that the difference between light and dark areas cannot be explained purely by changing the strength of a spectral absorption band in either carbon suboxide or ferric iron (Fe^{+++}).

As is indicated in Fig. 21 changing the particle size of a material can increase its reflectivity and also make it redder within a certain range of particle sizes. This characteristic results from transopaque behavior in a mineral. While none of the materials actually tested matched the Mars' curves it seems quite possible that an oxidized basalt could be found with the necessary properties.

In summary, the martian light and dark areas cannot be explained as simply different polymers of carbon suboxide. It may be possible to match the reflectivity characteristics of both light and dark areas with those of oxidized basalt. However, if this is the case there must be a difference in particle size as well as composition. But broad band reflectivity characteristics are not sufficiently unique to be able to exclude the possibility that the martian light and dark areas are covered or coated with materials whose existence or occurrence in this context is entirely unanticipated.

VII. SUMMARY AND FURTHER WORK

The spectral reflectivity of Mars have been studied for many decades by means of visual and instrumental methods. Differences have been observed in the spectral reflectivity of the light and dark planetary markings and have been attributed to differences in surface materials (eg. Pollack and Sagan 1969; Van Tassel and Salisbury, 1964; Plummer and Carson 1969). The spectral reflectivity differences are also reported to change seasonally and Sagan and Pollack (1969) are among those advocating the transport and deposition of dust by the martian winds as the cause of changes that take place in the martian features. Adams and McCord (1969) have obtained observational evidence which conflicts with this interpretation. They find that models of local seasonal condensation of ice or moisture or of growth of macroscopic very dark gray vegetation satisfy their data.

In the present study, the spectral characteristics of Mars have been studied at greatly improved spatial resolution and using sophisticated computer methods to analyse the vastly increased amount of photometric data. The first meaningful attempts to take account of the effect of local geometry on the measured reflectivities have also been made. But perhaps the most significant innovation is the use of high resolution photographic photometry in discriminating surface spectral reflectivity differences from those produced by geographic variations in the scattering atmosphere. Color-color and color-reflectivity diagrams were important in accomplishing this and were also valuable in making a comparison with the moon and with martian surface models proposed by other investigators. It is concluded that the spectral reflectivity differences between

the light and dark areas of the martian surface cannot be explained in terms of different polymer states of carbon suboxide as suggested by Plummer and Carson (1969). A difference in the particle size of oxidized basalt as proposed by Adams and McCord (1969) is a possible explanation but the observations are not sufficiently diagnostic for a positive identification.

Three color techniques have powerful future applications in the study of Mars by the Mariner Mars 1971 orbiting spacecraft. Of foremost interest are the temporal variations in the martian features and their study is a prime objective of the 1971 mission. Earth-based observations demonstrate that three color imagery permits different kinds of variable phenomena to be recognized (yellow clouds, blue clouds, the wave of darkening, the blue clearing). It is essential that the same kind of observations be made from the spacecraft in order to adequately characterize the feature variations. Other kinds of imaging and non-imaging information will be necessary, however, to distinguish atmospheric from surface phenomena.

TABLES AND ILLUSTRATIONS

TABLE 1

GEOMETRICAL PARAMETERS OF MARINER 7 IMAGES ANALYZED

Picture Number	Alternate Designation	Camera	Filter	Sub-spacecraft Lat°	Sub-spacecraft Long°	Sub-solar Lat°	Sub-solar Long°	Noran[3] °	Phase °	Radius Pixels
7F67		B(FE)[1]	minus blue	-8.96	19.76	-9.03	42.01	76.3	22.77	--
R-05	R 7D702445	A(LFE)[2]	red	-9.41	10.12	-9.28	29.05	83.5	20.83	219.5
G_1-05	G_1 7D702462	A(LFE)[2]	green	-9.47	9.82	-9.28	28.70	83.7	20.86	222.0
B-05	B 7D702474	A(LFE)	blue	-9.53	9.52	-9.28	28.36	84.0	20.90	224.5
G_2-06	G_2 7D702491	A(LFE)	green	-9.59	9.22	-9.28	28.02	84.4	20.90	227.0

1. Pictures taken by the narrow angle (B) camera during the far encounter (FE) picture sequence.
2. Pictures taken by the wide angle (A) camera during the late far encounter (LFE) picture sequence.
3. NORAN is the angle that the rotation axis of the planet makes with the horizontal scan lines.

TABLE 2 (a) SUMMARY OF BROAD BAND REFLECTIVITIES DETERMINED BY MARINER 7

Feature Name	Location Lat.	Location Long.	Area km^2	Illumination & viewing conditions[2] cos i	cos ε	Local Mars Time	R_1	G_1	B	G_2
1. Moab	+15.0°	17.5°E	328,000	0.89	0.89	11:20 a.m.	.159	.113	.093	.120
2. Oxia Palus	+7.0°	341.5°E	86,000	0.65	0.84	8:52 a.m.	.1145	.0935	.083	.099
3. Thymiamata	-1.0°	346.0°E	197,000	0.73	0.90	9:10 a.m.	.1275	.098	.086	.1055
4. Edom	-1.0°	17.5°E	264,000	0.97	0.98	11:16 a.m.	.154	.112	.0935	.1205
5. Margaritifer Sinus	-10.0°	334.0°E	341,000	0.60	0.82	8:22 a.m.	.0945	.082	.077	.087
6. Meridiani Sinus	-9.0°	0°E	321,000	0.88	0.99	10:06 a.m.	.104	.0845	.0785	.0905
7. Sabaeus Sinus	-11.5°	16.5°E	221,000	0.97	0.99	11:12 a.m.	.115	.090	.0825	.096
8. Deucalionis Regio	-18.0°	10.0°E	318,000	0.94	0.99	10:46 a.m.	.1485	.109	.090	.113
9. Pandora Fretum	-25.0°	349.0°E	270,000	0.75	0.90	9:22 a.m.	.1175	.0935	.084	.099

1. Total reflectivity = reflectivity of surface and atmosphere under the specified illumination and viewing conditions
2. Phase angle = $21^\circ \pm 1^\circ$

TABLE 2 (b)

AVERAGE GREEN BROAD BAND REFLECTIVITY AND COLOR RATIOS FOR SELECTED MARTIAN FEATURES

	Feature Name	$G=\frac{G_1 + G_2}{2}$	$\frac{R}{G}$	$\frac{R}{G}$
1.	Moab	.1175	1.350	.786
2.	Oxia Palus	.0995	1.190	.861
3.	Thymiamata	.102	1.250	.848
4.	Edom	.1165	1.325	.802
5.	Margaritifer Sinus	.0845	1.115	.912
6.	Meridiani Sinus	.0875	1.188	.897
7.	Sabaeus Sinus	.093	1.190	.886
8.	Deucalionis Regio	.111	1.335	.813
9.	Pandora Fretum	.096	1.220	.872

TABLE 3. COMPARISON OF BROADBAND REFLECTIVITY DETERMINED BY MARINER 7 WITH GROUND BASED SPECTRAL REFLECTIVITY MEASUREMENTS

	Reflectivity				Color Ratio		Normalised Green Reflectivity	Relative Reflectivity and Color		
	R	G-1	G-2	B	$RG = R/G_{AV}$	$BG = B/G_{AV}$	$D(\lambda=.525\mu)$ [1]	$\frac{G_{AV}(\text{light})}{G_{AV}(\text{dark})}$ [2]	$\frac{RG\ (\text{light})}{RG\ (\text{dark})}$	$\frac{BG\ (\text{light})}{BG\ (\text{dark})}$
Mariner 7										
Light Area Moab	.159	.113	.120	.093	1.350	.786	.15	1.28	1.135	.88
Dark Area Meridiani Sinus	.104	.0845	.0905	.0785	1.188	.897				
Predicted from ground based data	.194	.127	.122	.084	1.56	.674	.19 (Dollfus)	1.29	1.18	.89
Light Area Arabia										
Dark Area Syrtis Major	.127	.097	.095	.073	1.32	.758				

1. $D(\lambda) = \frac{B_{\perp}(\lambda;\ i,\ e,\ \alpha = 0)}{B_{\perp\ \text{lambert}}(\lambda;\ i,\ e,\ \alpha = 0)}$ is the diffusion factor defined by Dollfus (1965). The Mariner measurements have been converted to $D(\lambda)$ using the Minnaert law and the dependence of brightness on phase angle given by Dollfus (1965) to permit a comparison with Dollfus' estimate of $D(\lambda)$.

2. The Mariner data were corrected for limb darkening using the Minnaert law. The McCord data were taken under very similar local geometry and do not require correction.

TABLE 4. MODEL A - WAVELENGTH DEPENDENT SURFACE PHOTOMETRIC FUNCTION
NO ATMOSPHERIC SCATTERING

PHOTO-METRIC CONSTANT C_1	HAZE REFLECT.	MINNAERT PARAM. K			DATA PARAMETERS				REFLECTIVITY/COLOR COEFFICIENTS	
					LIGHT AREA		DARK AREA			
		R (.585)	G [1] (.525)	B (.465)	G_{os}	R_{os}/B_{os}	G_{os}	R_{os}/B_{os}	D_1	D_2
0	0	0.60	0.60	0.60	.1145	1.65	.0938	1.32	.0628	.0110
5/6	0	0.65	0.60	0.55	.1145	1.66	.0938	1.34	.0647	.0073
10/6	0	0.70	0.60	0.50	.1145	1.675	.0938	1.36	.0657	.0044
15/6	0	0.75	0.60	0.45	.1145	1.69	.0938	1.38	.0668	.0017

1. Based on measurements of Young and Collins (1971)

TABLE 5. MODEL B - SURFACE PHOTOMETRIC FUNCTION
INDEPENDENT OF WAVELENGTHS, OPTICALLY THIN WHITE HAZE

OPTICAL DEPTH τ (λ = .525)	HAZE REFLECTIVITY			MINNAERT PARAM K			DATA PARAMETERS				REFLECTIVITY COLOR COEFFICIENTS	
		%					LIGHT AREA		DARK AREA			
	R (.585)	G (.525)	B (.465)	R (.585)	G (.525)	B (.465)	G_{os}	R_{os}/B_{os}	G_{os}	R_{os}/B_{os}	D_1	D_2
0	1.0	0	0	0.60	0.60	0.60	.1145	1.65	.0938	1.32	.0628	.0110
.036	1.3	1.3	1.3	0.68	0.68	0.68	.1030	1.75	.0820	1.38	.0568	.0036
.059	2.1	2.1	2.1	0.74	0.74	0.74	.0945	1.84	.0730	1.44	.0537	-.0043
.093	3.3	3.3	3.3	0.85	0.85	0.85	.0817	2.03	.0596	1.57	.0480	-.0157

TABLE 6. MODEL C - SURFACE PHOTOMETRIC FUNCTION
INDEPENDENT OF WAVELENGTHS, OPTICALLY THIN 'RAYLEIGH' HAZE

OPTICAL DEPTH $\tau(\lambda = .525)$	HAZE REFLECTIVITY			MINNAERT PARAM K			DATA PARAMETERS				REFLECTIVITY COLOR COEFFICIENTS	
							LIGHT AREA		DARK AREA			
	R (.585)	% G (.525)	B (.465)	R (.585)	G (.525)	B (.465)	G_{os}	R_{os}/B_{os}	G_{os}	R_{os}/B_{os}	D_1	D_2
0	0	0	0	0.60	0.60	0.60	.1145	1.65	.0938	1.32	.0628	.0110
0.014	.33	.50	.83	0.63	0.63	0.63	.1105	1.77	.0895	1.43	.0618	.0011
0.028	.67	1.0	1.67	0.66	0.66	0.66	.1055	1.93	.0845	1.57	.0583	-.0070
0.042	1.0	1.50	2.50	0.70	0.70	0.70	.099	2.14	.0775	1.76	.0566	-.0221

TABLE 7. COMPARISON OF MEASUREMENTS OF OPTICAL CHARACTERISTICS OF THE MARTIAN ATMOSPHERE AND SURFACE

EXPERIMENT	WAVE-LENGTH RANGE (microns)	ILLUMINATION & VIEWING CONDITIONS			MODEL OR CONCLUSION	ATMOSPHERE			SURFACE
		α	i	ϵ		OPTICAL DEPTH (.525μ)	NORMAL REFLECTANCE (.525μ)	$\frac{P^1(\alpha)}{P_R(\alpha)}$ [6*]	NORMAL REFLECTANCE (.525μ)
I. Mariner 69 Television									
a) Mariner 7 N.F.E. A Camera Pictures 1*	.46 to .58	22°	0° to 80°	0° to 70°	Model B White "Neutral" Haze, Rayleigh Phase Function	.084	3.0%	1.0	.09
					Model C Rayleigh Haze Rayleigh Phase Function	.042	1.5%	1.0	.10
b) Detached Limb Hazes (Near Encounter) 2*	.46 to .58	44.5°	25°	90°	White "Neutral" Haze, Non-Rayleigh Phase Function	.062	.7%	0.3	No Value
					Model 1 Uniform Layer				
					Model 2 Exponential Layer	.15	1.6%	0.3	No Value
c) Crater Shadow Studies 3*	.46 to .58	80.1°	38° to 90°	15° to 43°	White Haze with Rayleigh Phase Function Assumed	.3	10%	1.0	No Value
II. Mariner 69 Ultraviolet Spectrometer 4*	.28 to .40	62.5°	46.7°	41.9	Rayleigh Wavelength Dependence and Phase Function Inferred from Measurements	.012	.25%	1.0	.030
III. Earth Based Polarimetric 5*	Visible Light	-20°	0° to 30°	0° to 30°	Rayleigh Wavelength Dependence Inferred from Measurements. Rayleigh Phase Function Assumed.	.020	.40%	1.0	No Value Cited
IV. Clear Atmosphere	Visible Light	0°	0°	0°	Theoretical	.004	.08%	1.0	-

*1. Results of this study.
2. Leovy et al., 1971.
3. K. Blasius, Private communication, 1970.
4. Hord and Barth, 1970.
5. Dollfus, A., Proceedings of the Caltech-JPL Lunar and Planetary Conference (Sept. 13-18) 1965, p. 288.
6. Ratio of phase function (assumed or calculated) to the Rayleigh phase function.

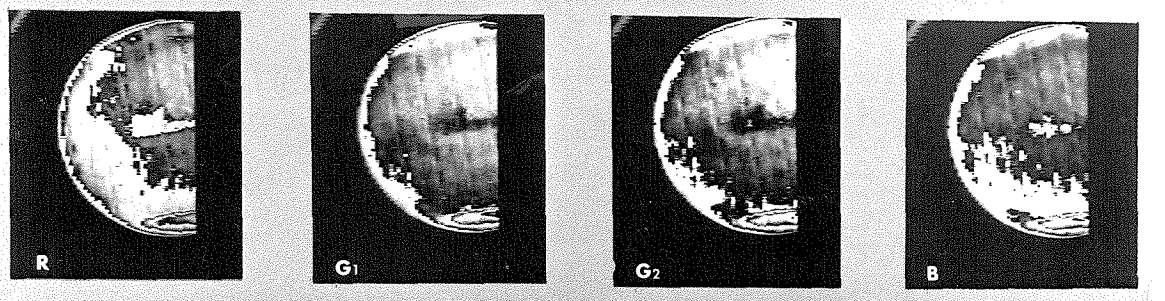

RAW DATA

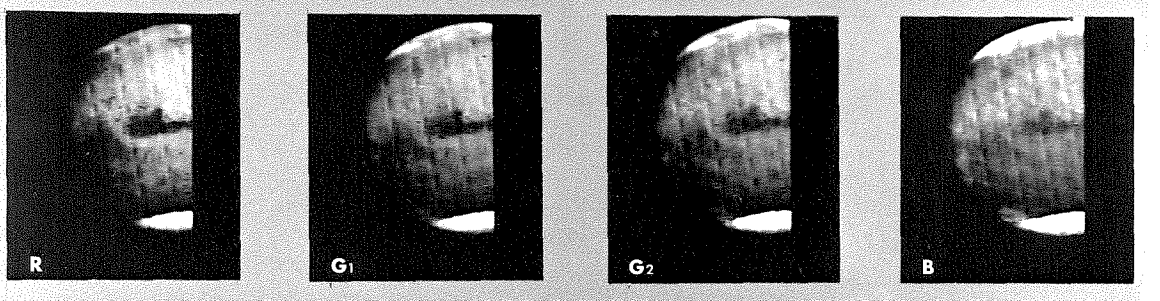

DATA BIT RESTORATION

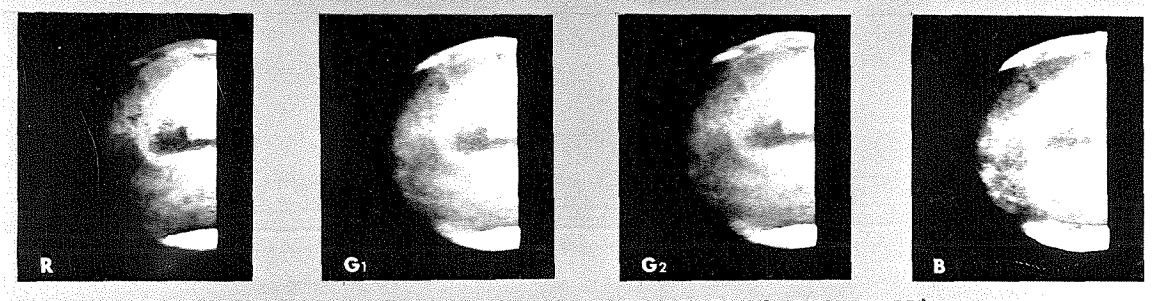

NOISE REMOVAL AND DECALIBRATION (ENHANCED)

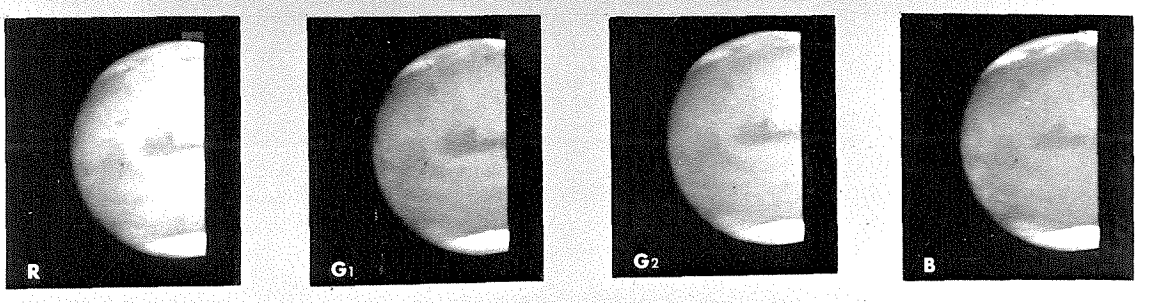

TRUE CONTRASTS

I. DECALIBRATION - CONVERSION OF RAW DATA TO PHOTOMETRIC FORM

Raw data (line 1) is first converted to eight-bit data (line 2) by the process of bit restoration. Coherent noise and other defects are then removed (line 3) and the data is finally converted to the photometric form (line 4) showing the planet in its true contrast.

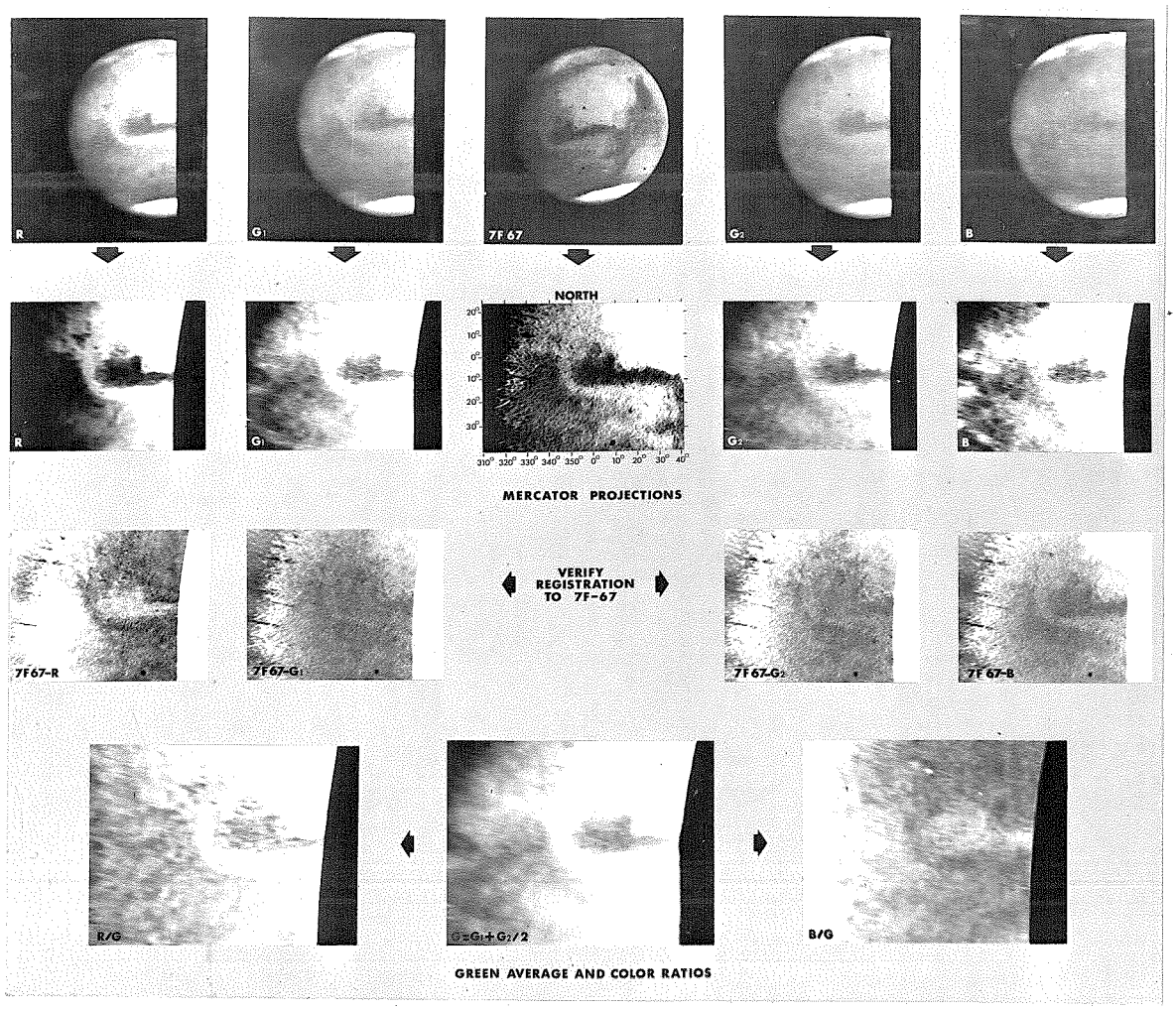

2. TRANSFORMATION OF PHOTOMETRIC IMAGES INTO MERCATOR COORDINATES

The decalibrated photometric images (line I) are converted into the mercator projection by means of the program GEOM. Minor shifts are applied to register these images to a mercator pr ojection of picture 7F67 which is based on more precise cartographic information. This reregistration is verified by forming difference pictures (line 3) and in line 4 the two green images (G_1 and G_2 are averaged and both the red and the blue image (R and B) are ratioed with this average.

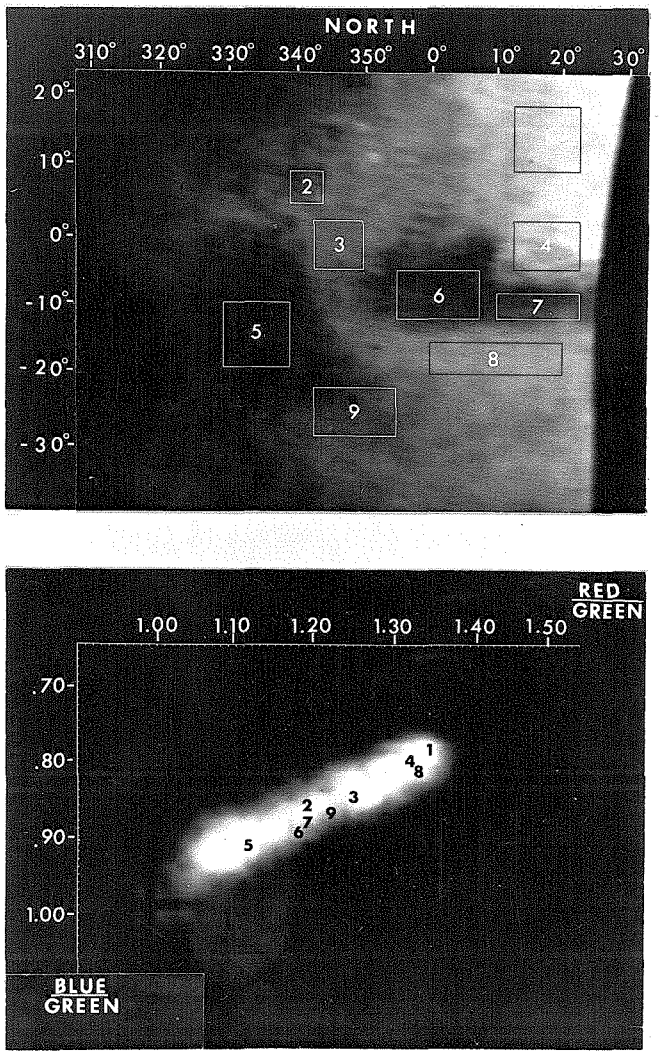

3. THE APPARENT COLOR RATIOS OF MAJOR MARTIAN FEATURES

Broad band reflectivities are averaged over the areas outlined within the classical martian features (top). The features are 1. Moab 2. Oxia Palus 3. Thymiamata 4. Edom 5. Margaritifer Sinus 6. Meridiani Sinus 7. Sabaeus Sinus 8. Deucalionis Regio 9. Pandora Fretum. The values of the color ratios for each of these areas are denoted by the position of these numbers in the plot of red/green ratio against blue/green ratio. The numbers are superimposed on a histogram of the color ratios of the entire region shown.

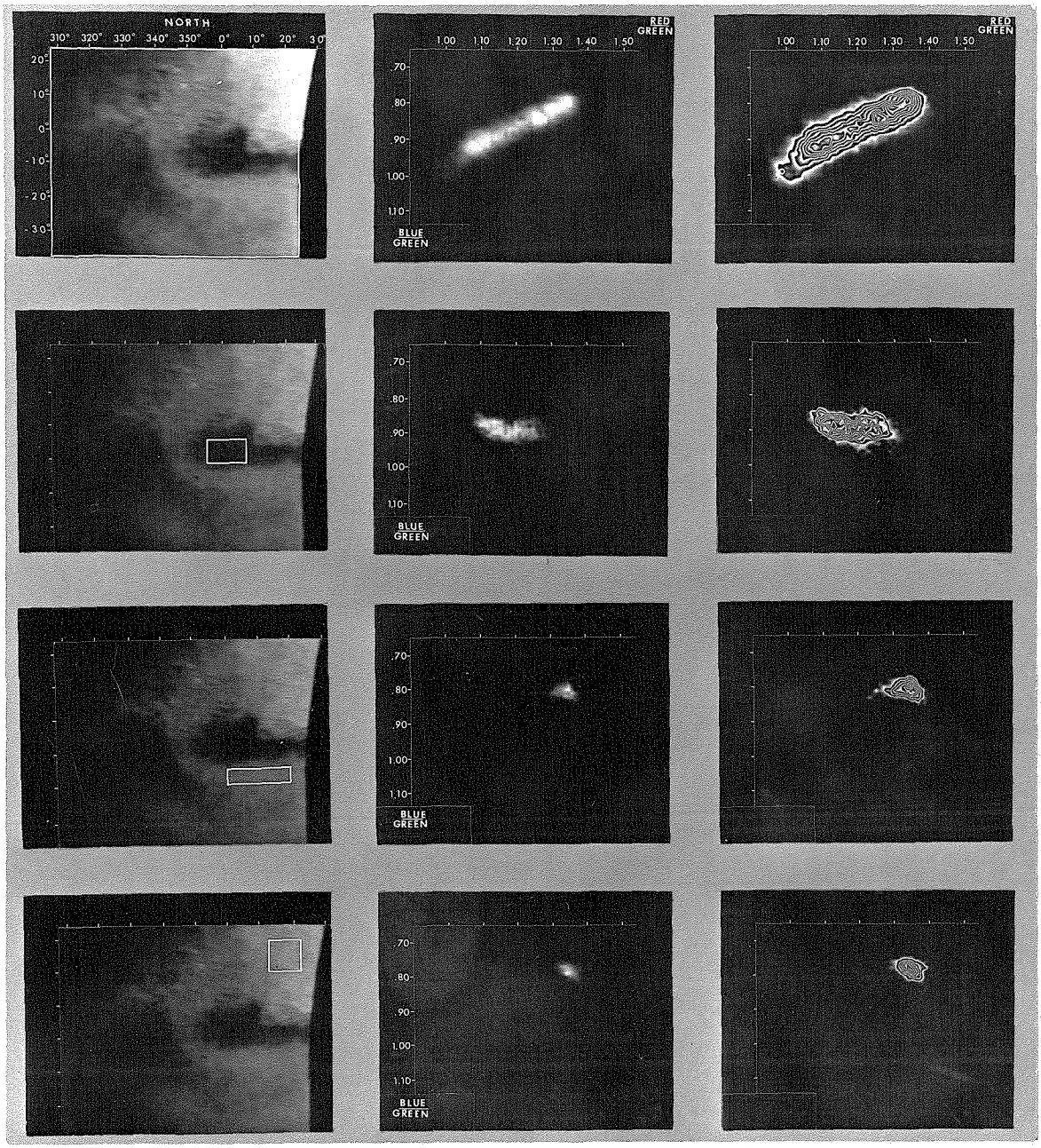

4. THE BIVARIATE DISTRIBUTION OF COLOR RATIOS WITHIN MARTIAN FEATURES SHOWN USING THE CLUSTR PROGRAM

Bivariate histograms of the color ratios RED/GREEN and BLUE/GREEN for each of the areas outlined (column 1) are displayed in Column 2. These histograms are contoured for better definition by truncating the two most significant bits in the histogram data (column 3). The areas outlined are line 1: entire region 20°N to 35°S, 310°E to 25°E; line 2: part of Meridiani Sinus; line 3: part of Deucalionis Regio; line 4: part of Moab. The large variation in color within Meridiani Sinus is attributed to the misregistration of small albedo features when forming color ratio data.

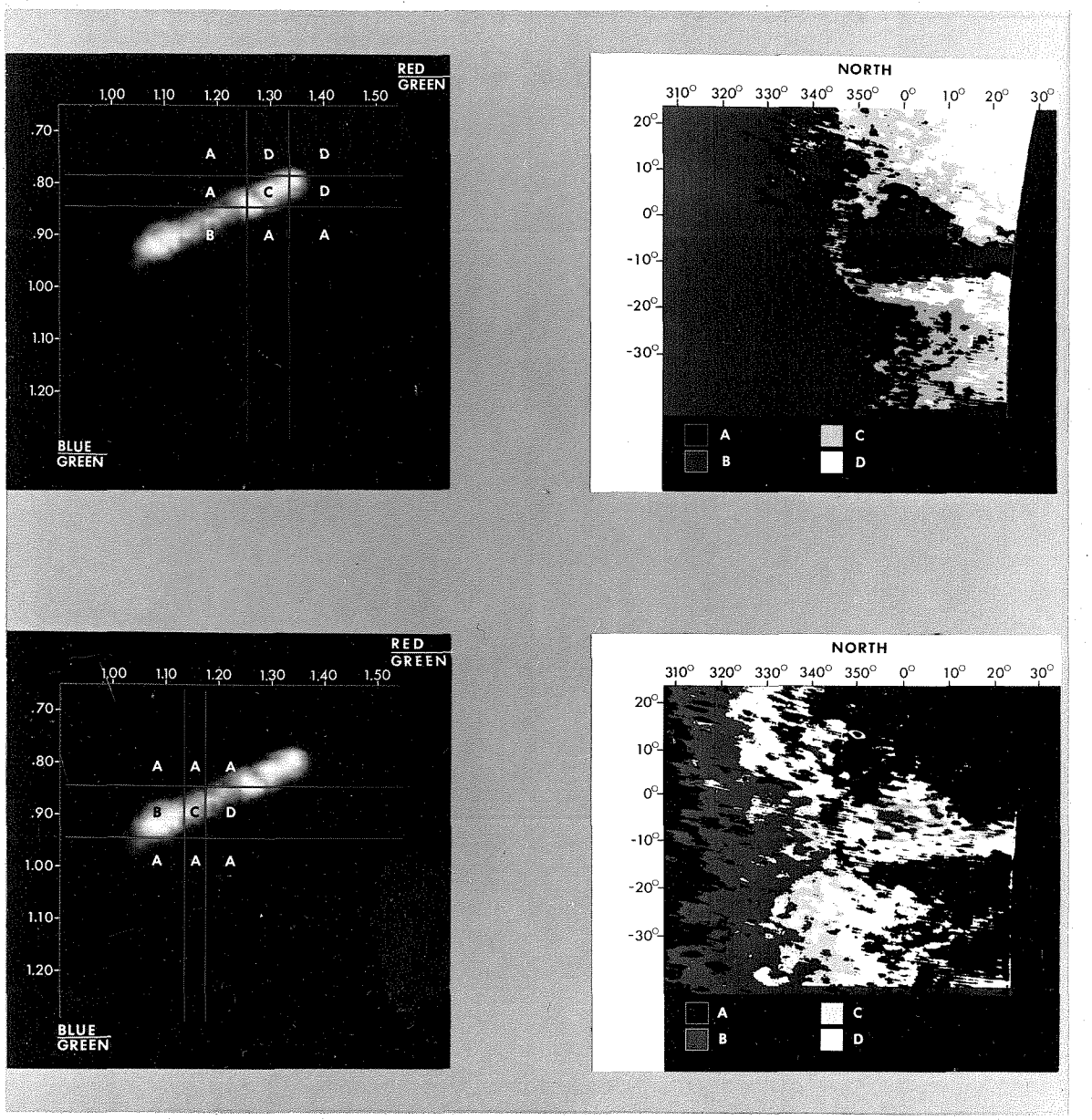

5. THE DISTRIBUTION OF COLOR GROUPS ON MARS SHOWN USING THE COLMAP PROGRAM

The martian areas which contribute to the nine different zones in the histograms (left) defined by the horizontal and vertical lines are denoted by different gray levels (A, B, C & D) in the mercator maps of Mars (right). In the first histogram–colormap pair the zones have been chosen on the basis of the histograms of Fig. 4 to optimally separate the regions Meridiani Sinus, Deucalionis Regio and Moab on the basis of color. In the second colormap pair the zones are chosen to examine color variations within Meridiani Sinus and to display the increase in blue reflectivity (relative to red and green reflectivity) in the direction of the morning terminator (west). This increase is attributed at least in part to the effect of the local geometry of illumination and viewing.

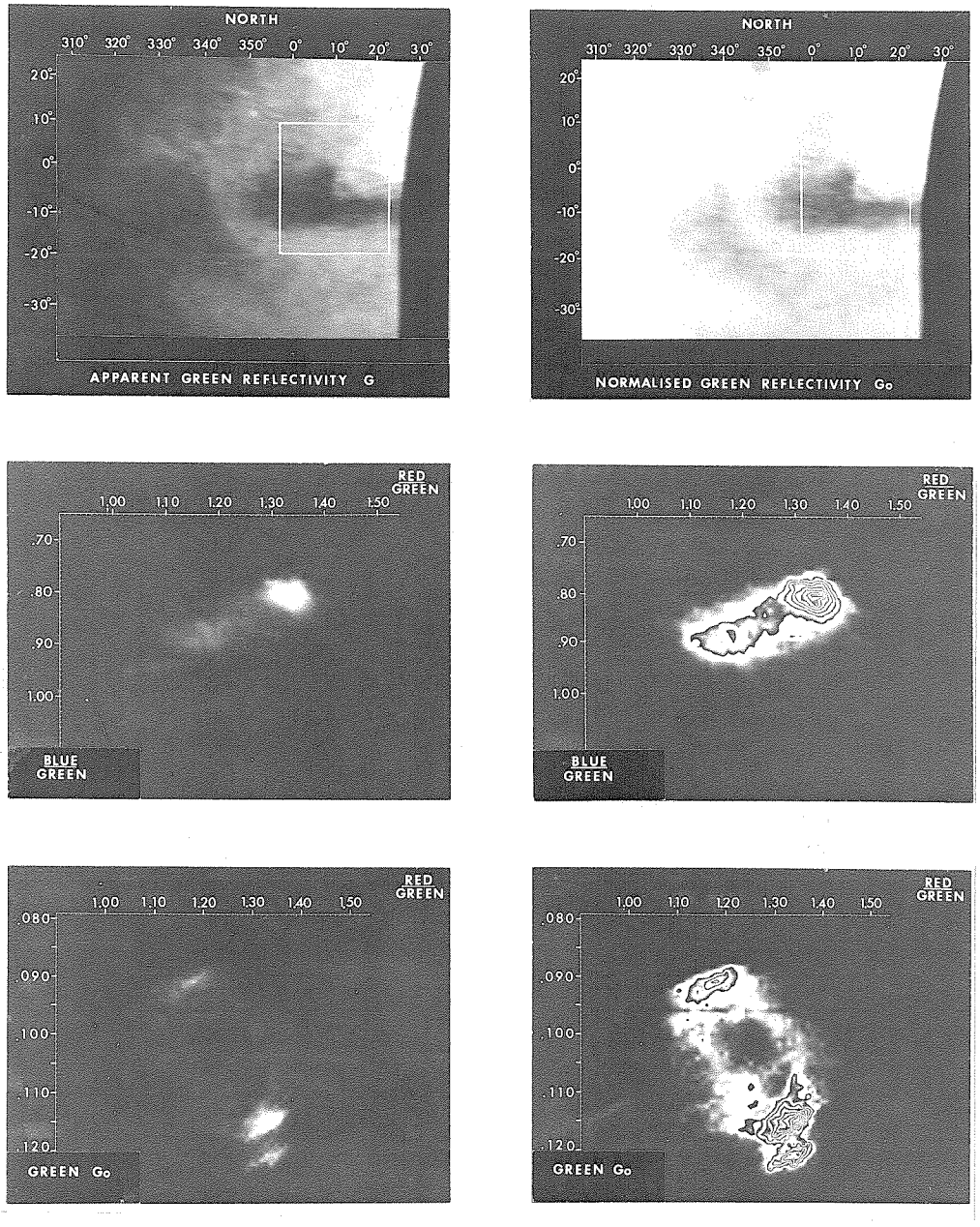

6. THE RELATIONSHIP BETWEEN R/G AND B/G AND R/G AND GO FOR MARTIAN FEATURES NEAR THE CENTER OF THE DISC

Near the center of the disc (sub-spacecraft point) the color variation due to changes in local geometry is small and dominated by color variation due to geographic changes in the atmosphere and/or surface. The bivariate distributions of RED/GREEN and BLUE/GREEN color ratios are displayed in line 2. The mercator image top right (Go) is a photometrically corrected version of the measured green reflectivity (G). The photometric correction was performed using the Minnaert photometric law. The bivariate distribution of RED/GREEN and Go (line 3) indicates a strong correlation. The minimum near Go=.102, R/G= .124 is an artifact of residual misregistration.

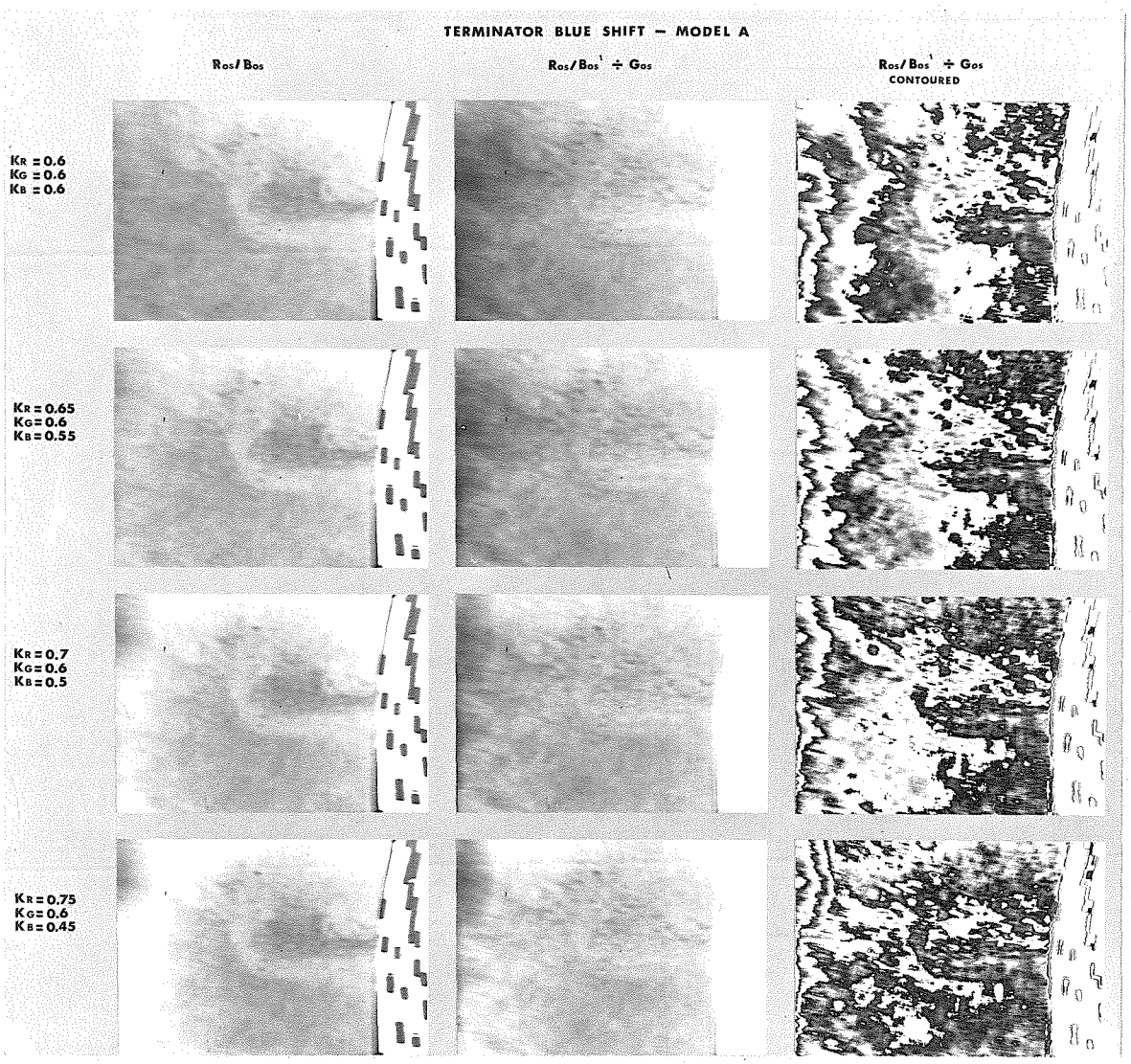

7. TERMINATOR BLUE SHIFT MODEL A, NO HAZE, WAVELENGTH DEPENDENT PHOTOMETRIC FUNCTION

The increase in blue reflectivity (relative to green) towards the morning terminator is modeled by a wavelength dependent photometric function. Atmospheric scattering is assumed to be negligible and the Red/Blue color proportional to green reflectivity when these are measured under standard illumination and viewing conditions (R_{os}/B_{os} and G_{os}). The value of R_{os}/B_{os} is calculated for different degrees of photometric wavelength dependence (column 1) and is then converted to $(R_{os}/B_{os})'$ prior to forming a ratio image with Go (column 2). If the photometric wavelength dependence is correctly chosen then there will be no gross change in the brightness of this ratio image to either the east or west. In column 3 the ratio images are contoured to improve the discrimination of trends. The photometric wavelength dependence used in line 4 (k_R=0.75, k_G=0.6, k_B=0.45) is considered optimal. The small markings at the right side of image are spurious.

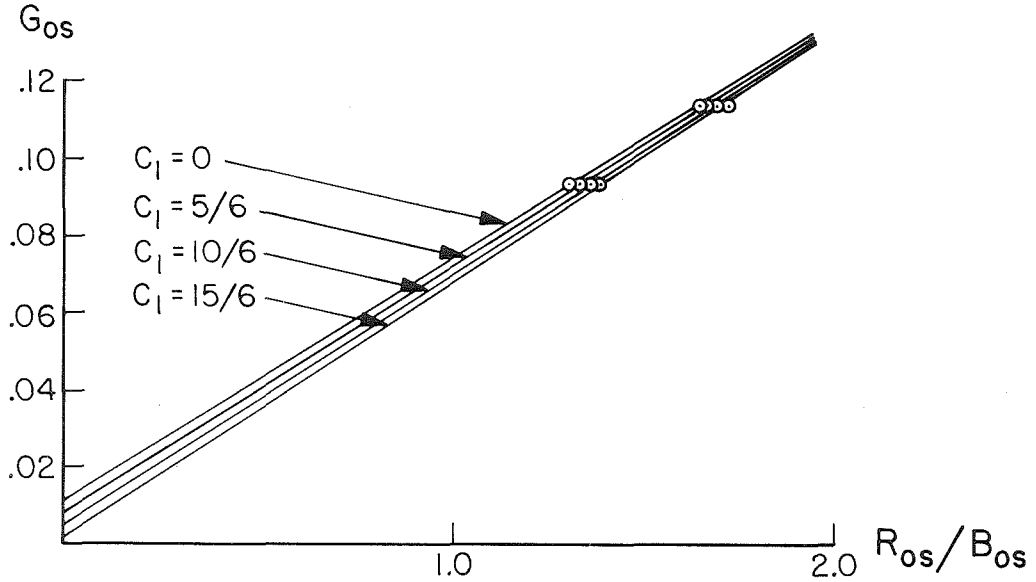

8. CONTRAST ADJUSTMENT FACTORS FOR MODEL A

For each value of C_1 (photometric wavelength parameter) the values of R_{os}/B_{os} and G_{os} are shown for a light area (Deucalionis Regio) and a dark area (Meridiani Sinus). These areas are near the center of the martian disc and the effect of local geometry on the relative values of color ratios and reflectivities is small. It is assumed that the linear relationship between color and albedo so defined applies to all the features in the entire region studied. Constants D_1 and D_2 defining this linear relationship are listed in table 4.

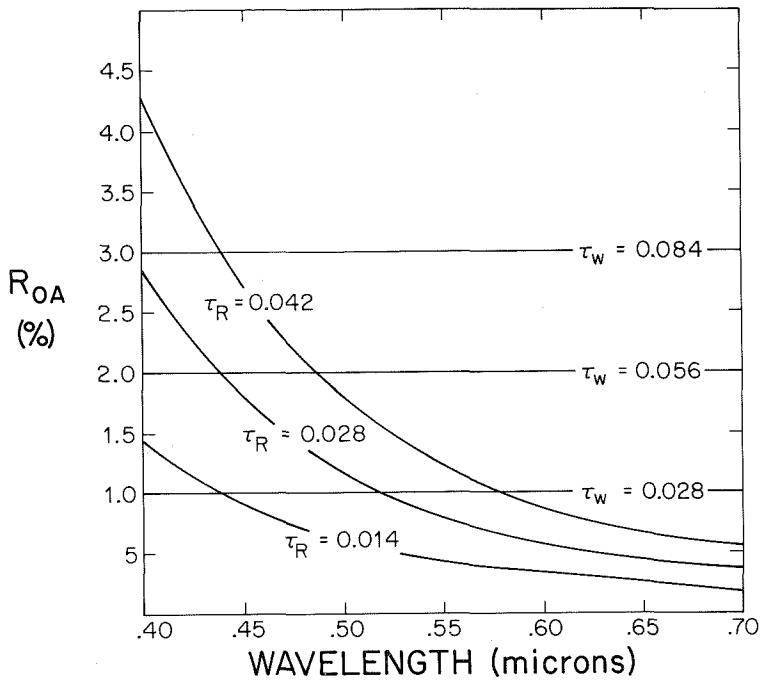

9(a) MODEL HAZES

The wavelength dependence of the normal reflectivity of the uniform haze levels tested in Models B and C.

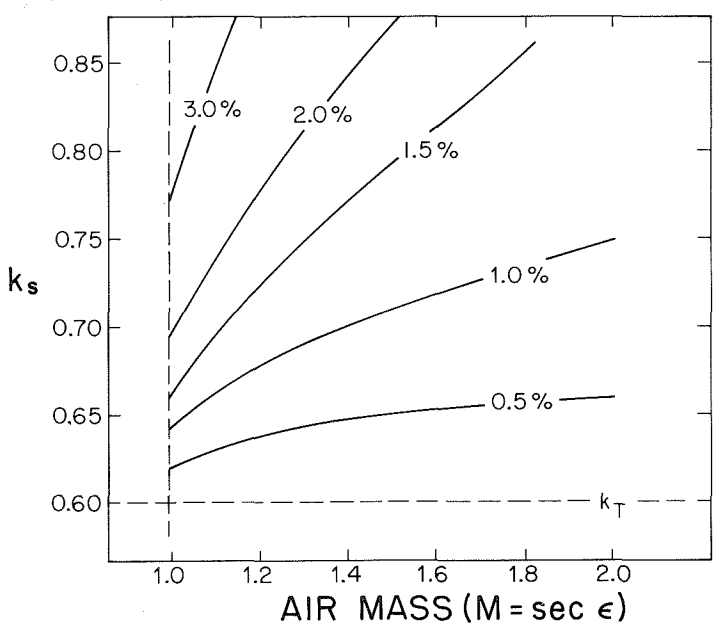

9(b) DEPENDENCE OF K_S ON HAZE LEVEL

The value of k_s (the Minnaert parameter for the martian surface alone) is shown as a function of air mass (M=sec ϵ) and the assumed normal haze reflectivity. K_t is the Minnaert parameter which applies to the total light reflected from the planet. When the haze level is assumed to zero k_t and k_s are equivalent.

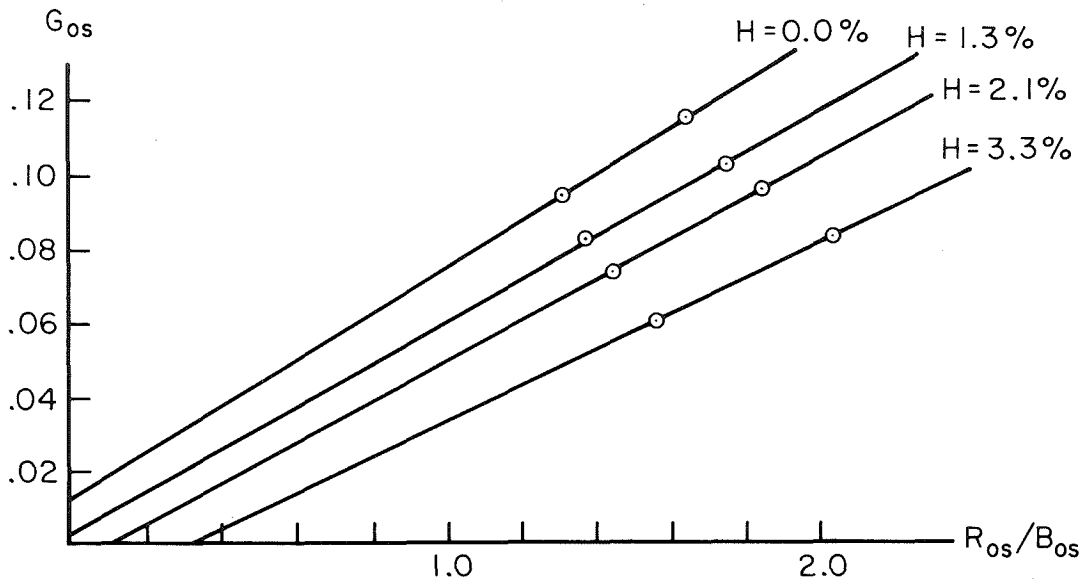

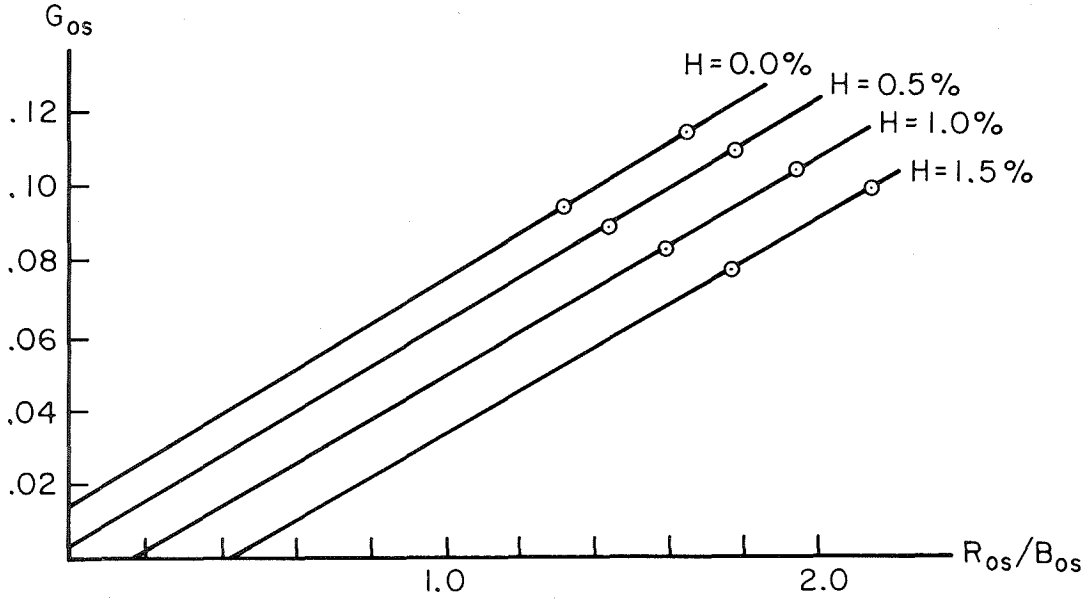

10. CONTRAST ADJUSTMENT FACTORS FOR MODELS B AND C

For each value of H (normal haze reflectivity) the values of R_{os}/B_{os} and G_{os} are shown for a light area (Deucalionis Regio) and a dark area (Meridiani Sinus). These areas are near the center of the Martian disc and the effect of local geometry on the relative values of color ratios and reflectivities is small. It is assumed that the linear relationship between color and albedo so defined applies to all the features in the entire region of Mars studied. Constants D_1 and D_2 defining this linear relationship are listed in Tables 5 and 6.

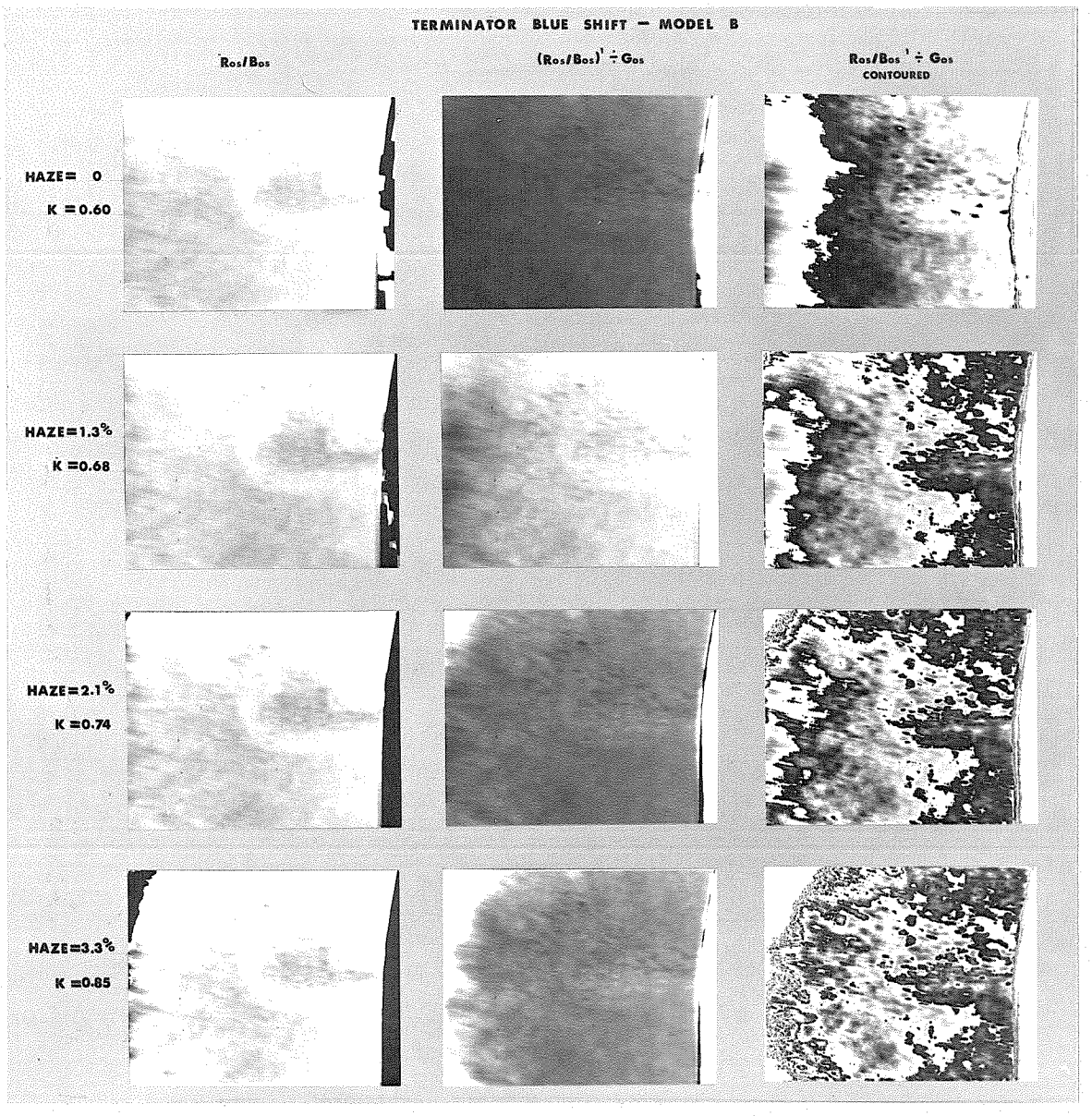

II. TERMINATOR BLUE SHIFT MODEL B, UNIFORM 'WHITE' HAZE, WAVELENGTH INDEPENDENT SURFACE PHOTOMETRIC FUNCTION

The increase in blue reflectivity (relative to red and green) towards the morning terminator is modeled by a uniform white haze layer. The surface photometric function is assumed to be independent of wavelength and the Red/Blue color proportional to green reflectivity (when measured under standard illumination and viewing conditions. The value of R_{os}/B_{os} is calculated for different values of the haze density (column 1) and is then converted to $(R_{os}/B_{os})'$ prior to forming a ratio image with Go (column 2). If the haze density is correctly chosen then there will be no gross change in the brightness of this ratio image to either the east or west. In column 3 the ratio images are contoured to improve the discrimination of trends. No haze level can be found which provides an adequate balance over the entire field.

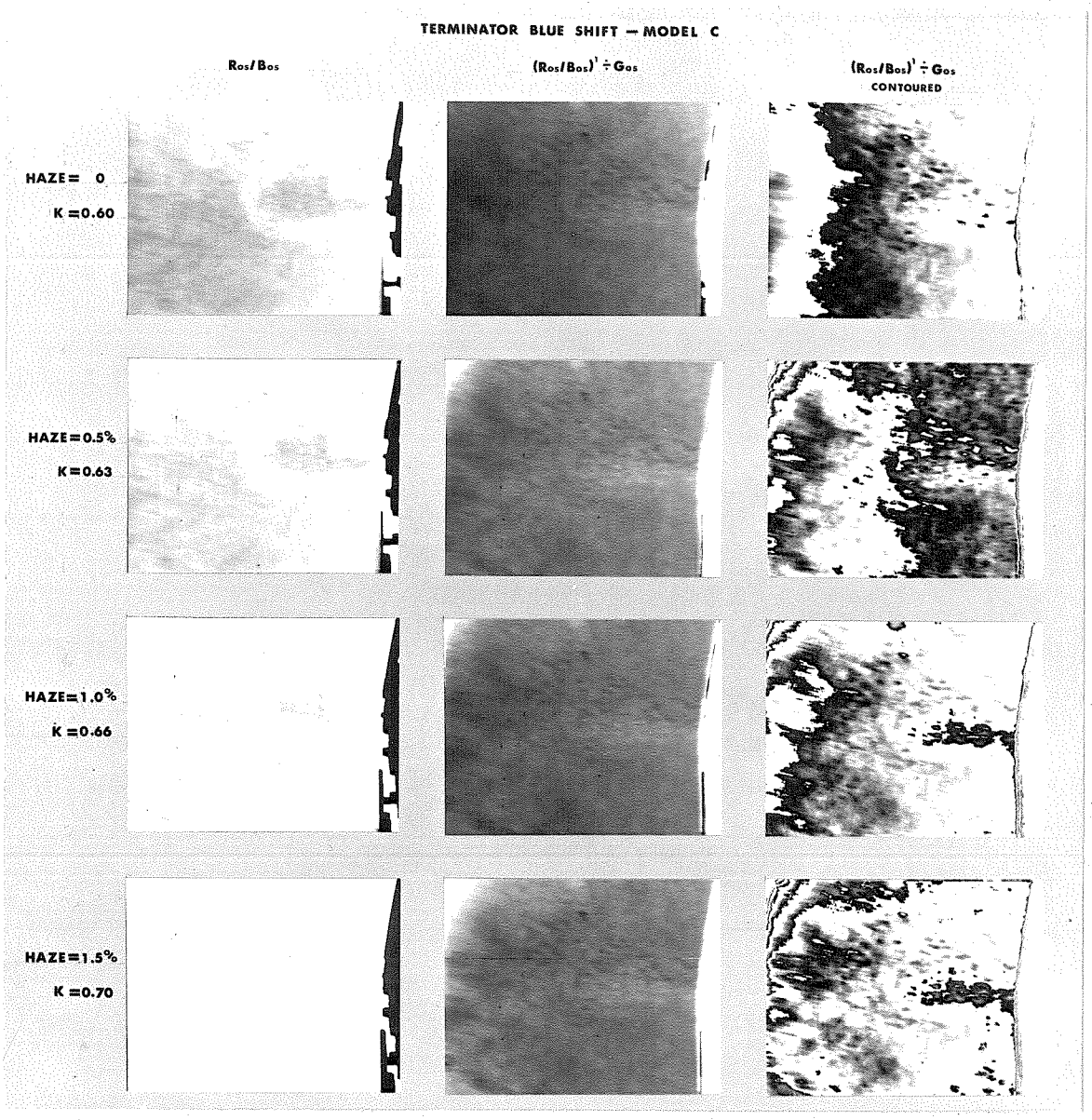

12. TERMINATOR BLUE SHIFT MODEL C, UNIFORM 'BLUE' RAYLEIGH HAZE, WAVELENGTH INDEPENDENT SURFACE PHOTOMETRIC FUNCTION

The increase in blue reflectivity (relative to red and green) towards the morning terminator is modeled by a uniform blue rayleigh scattering haze layer. The surface photometric function is assumed to be independent of wavelength and the Red/Blue color proportional to green reflectivity (when measured under standard illumination and viewing conditions. The value of R_{os}/B_{os} is calculated for different values of the haze density (column 1) and is then converted to (R_{os}/B_{os}) prior to forming a ratio image with Go (column 2). If the haze is correctly chosen then there will be no gross change in the brightness of this ratio image to either the east or west. In column 3 the ratio images are contoured to improve the discrimination of trends. The haze level used in line 4 provides an acceptable match to the data.

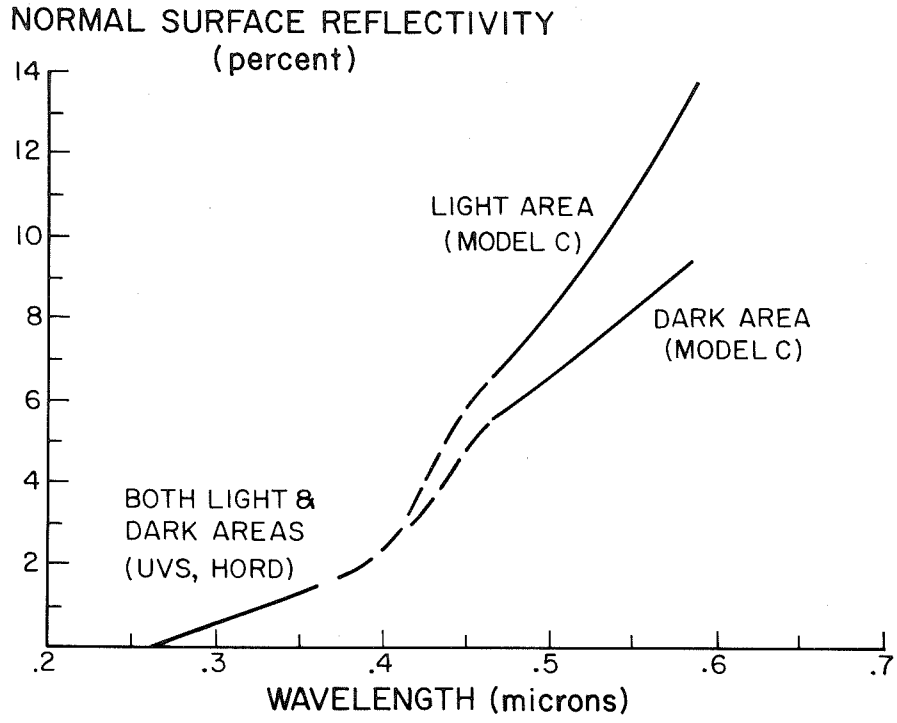

13. NORMAL REFLECTIVITY OF THE SURFACE OF MARS

(a) The surface reflectivity of Mars assumed in the model of Hord and Barth (1971) for the wavelength range 0.26 to 0.36 microns is compared with that derived from visible for wavelength range 0.465 to 0.585 microns.

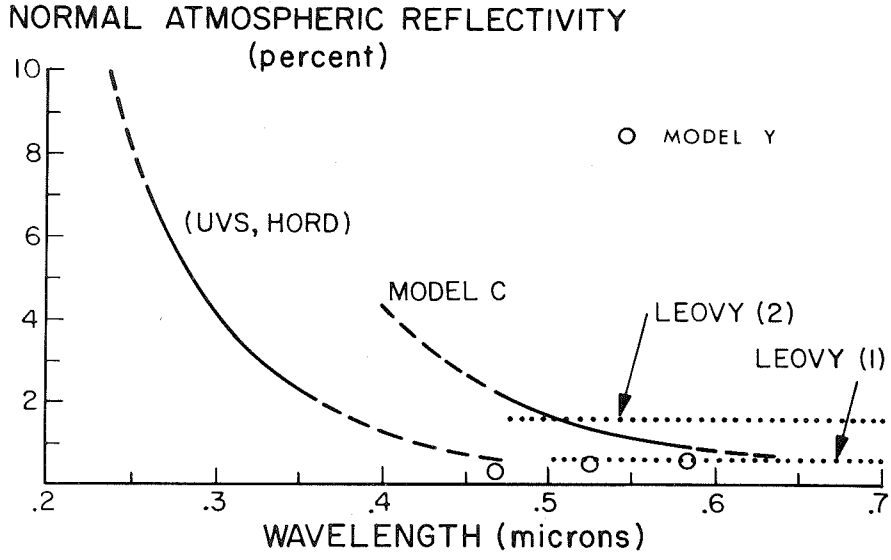

13. NORMAL REFLECTIVITY OF THE MARTIAN ATMOSPHERE BASED ON MODEL C AND THE HORD AND LEOVY MODELS

(b) For Model C and the Hord model extrapolation over a wider wavelength range is achieved using the Rayleigh law. Model Y depicts the haze reflectivity for the Moab region inferred from Late Far Encounter measurements.

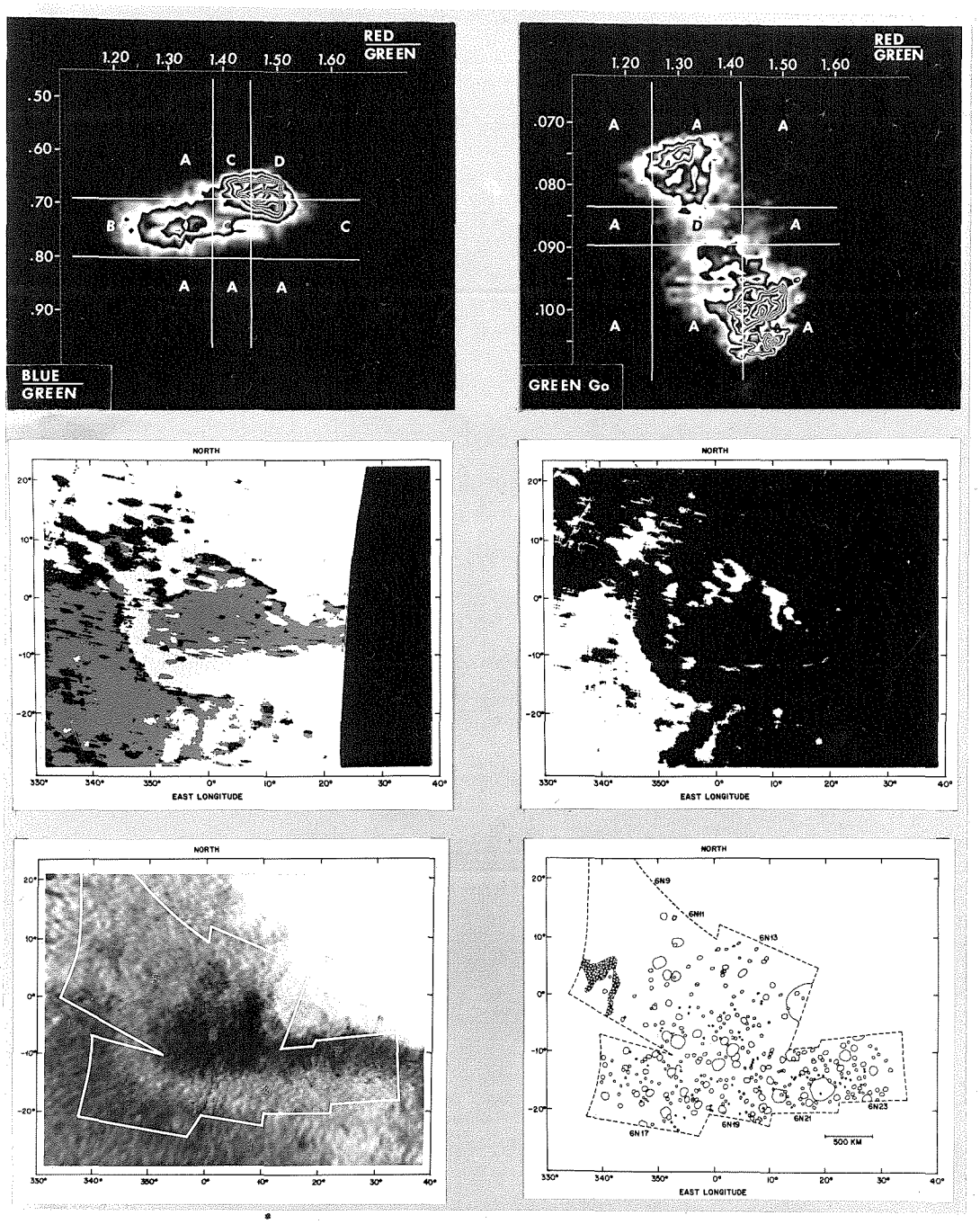

.14. COLOR AND ALBEDO DIFFERENCES BETWEEN MARTIAN FEATURES

The color ratio image used in forming the histogram (b) (top right) has been reregistered in order to remove the central minimum (Fig. 6) which is an artifact of misregistration. Using the program COLMAP the precision of this registration is verified in (d) center right) where the width of the transition zone around Meridiani Sinus is minimized.

The histogram and colormap (top left (a) and left center (c)) show the distribution of color types that is obtained after correcting for local geometry with Model C. The distribution of craters on Meridiani Sinus and the surrounding light areas as measured in Mariner 6 near encounter pictures is shown in (e) and (f) (bottom left and bottom right).

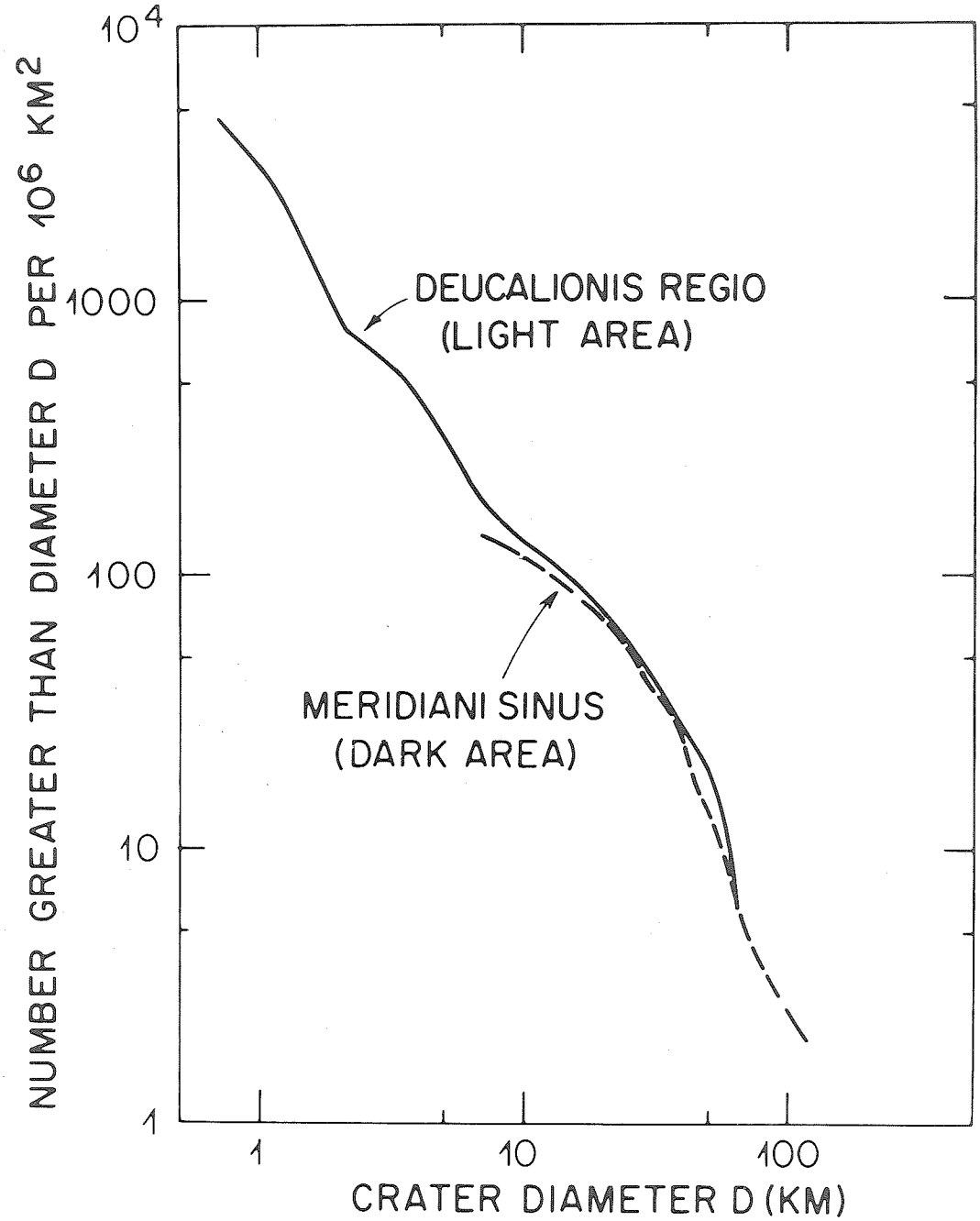

15. COMPARISON OF CRATER DENSITIES ON MERIDIANI SINUS AND DEUCALIONIS REGIO

The number of craters per $10^6 km^2$ with diameter larger than D is plotted for the dark area just north and light area just south of the Meridiani Sinus-Sabaeus Sinus/Deucalionis Regio boundary. Frames 6N13, 6N19 and 6N21 were used in compiling these crater size-frequency distributions. No B-frames were located in the dark area near the boundary; therefore, counts for the dark do not include craters smaller than about 10 km. (Published as Fig. 9 in the Paper by Cutts et al 1971a).

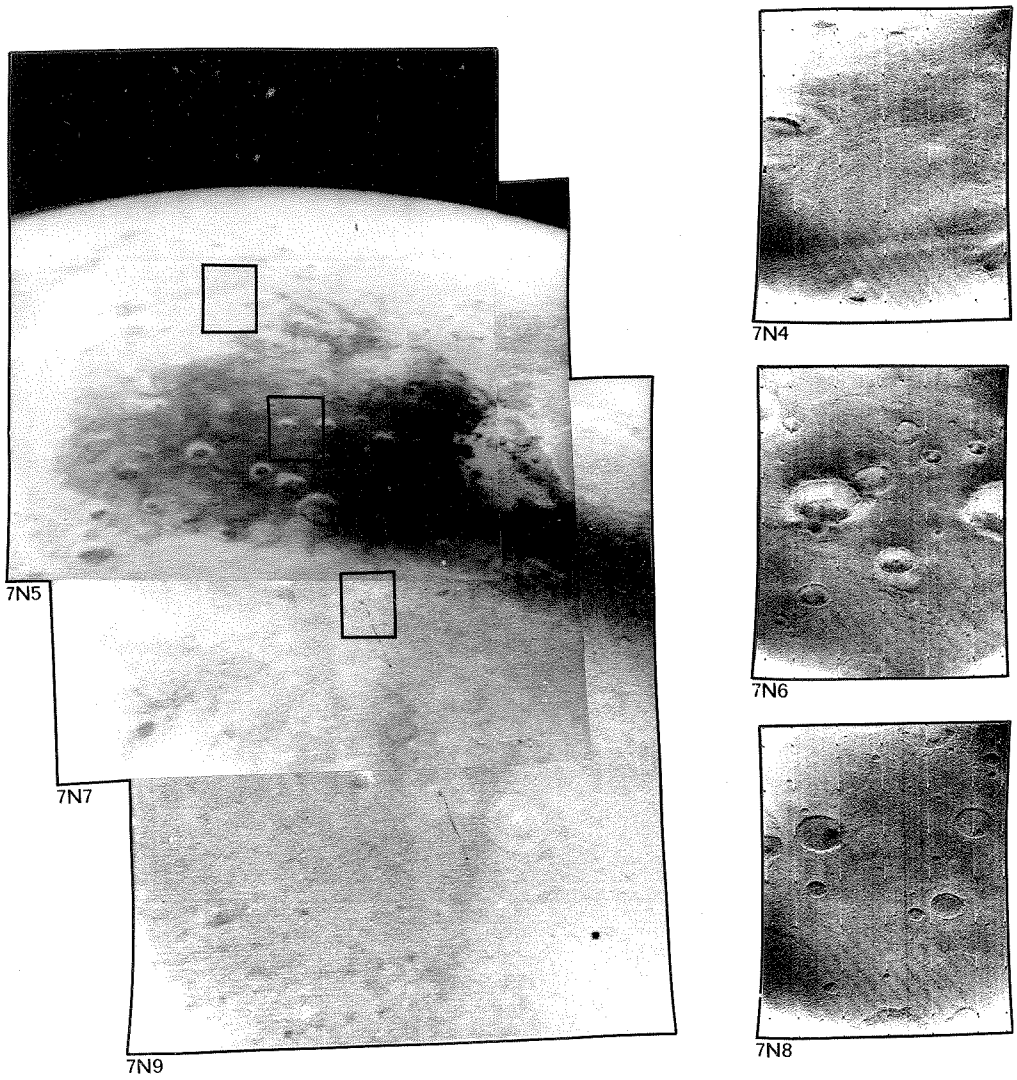

16. MOSAIC OF MARINER 7 NEAR ENCOUNTER PHOTOGRAPHS SHOWING AREAS WITH TYPE D_1, L_1 and L_2 REFLECTIVITIES

The direction of view is approximately NNW. The center of the lower edge of 7N9 is located at 15°E, 35°S; the center of the limb in 7N5 is at 350°E, 35°N. The dark area, (type D reflectivity area) Meridiani Sinus-Sabaeus Sinus lies along the equator, the light (type L_1 reflectivity area) Deucalionis Regio is south of this and the light (type L_2 reflectivity area) Moab is in the northeast corner of the mosaic. The crater, Edom, is in the northeast corner of 7N9. The east-west dimension of the mosaic ranges from 1200 km across the base of 7N9 to about 2000 km along the limb. The solar elevation angle ranges from 90° in Meridiani Sinus to 48° in the southern part of 7N9. Positions of the B-frames, 7N4, 6, and 8, are outlined in the mosaic. The A-frames 7N5, 7, and 9 were taken with red, green and blue filters respectively. As the contrast of light and dark markings is highest in the red and lowest in the blue, these pictures have been contrast-enhanced differently before assembling the mosaic. (Published as Fig. 8 in the Paper by Cutts et al 1971a).

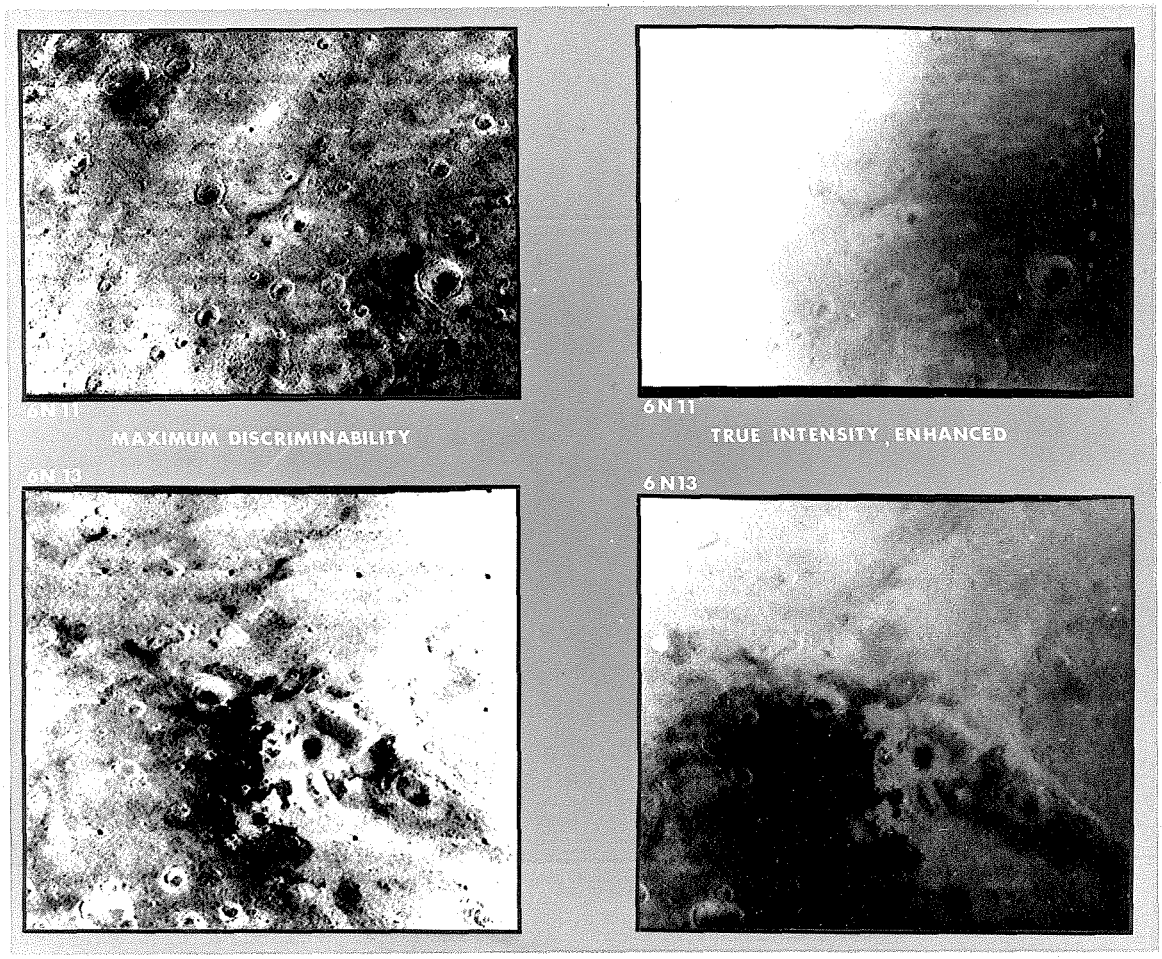

17. MARINER 6 FRAMES OF THE NORTHERN BOUNDARY OF MERIDIANI SINUS

Frames 6N11 and 6N13 display the variation in the planimetric character of a light/dark boundary and the changed appearance of albedo markings in craters across that boundary. The large crater Edom is located in the light area at the eastern edge of 6N13. Maximum discriminability versions have been processed so as to suppress regional albedo variations and to drastically enhance small scale variations in intensity. Thus light/dark transitions are less easily displayed on those versions, whereas albedo variations within craters are easily seen. The true intensity versions are included to better display the distribution of light and dark regions. The solar elevation angle varies from 52° in the southwest corner of 6N11 to 14° in the northeast edge of 6N13. The east-west dimensions of the sections of each frame shown is about 800 km. (Published as Figure 8 in the paper by Cutts et al 1971a).

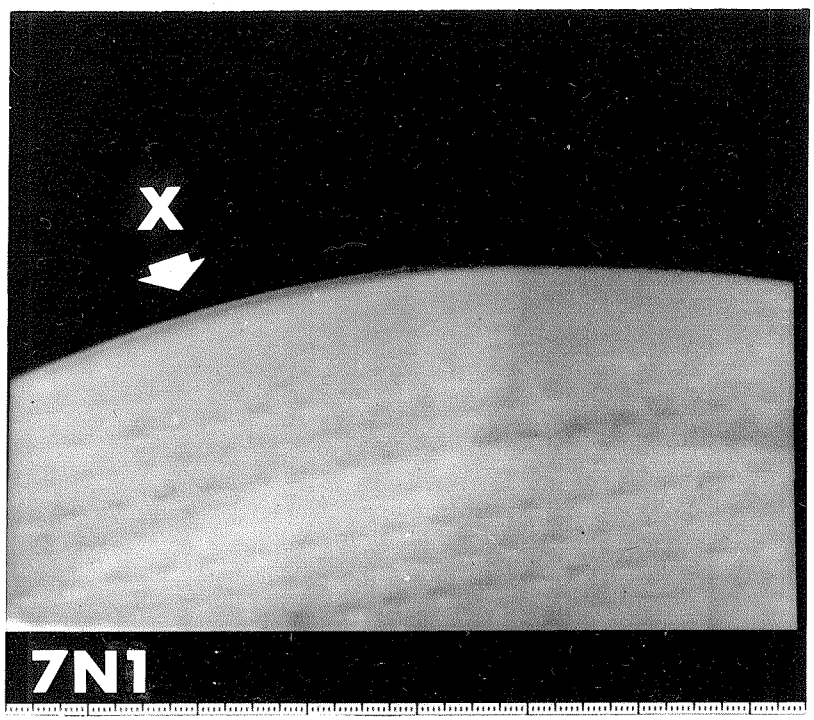

18. PICTURES OF THE MARTIAN LIMB 7N1 AND 7N7 SHOWING HAZE LAYERS ABOVE MOAB AND CHRYSE

Frame 7N1 and 7N7 show detached haze layers X and Y over the martian limb. These layers decrease in intensity to the east (right) and to the west (left) respectively.

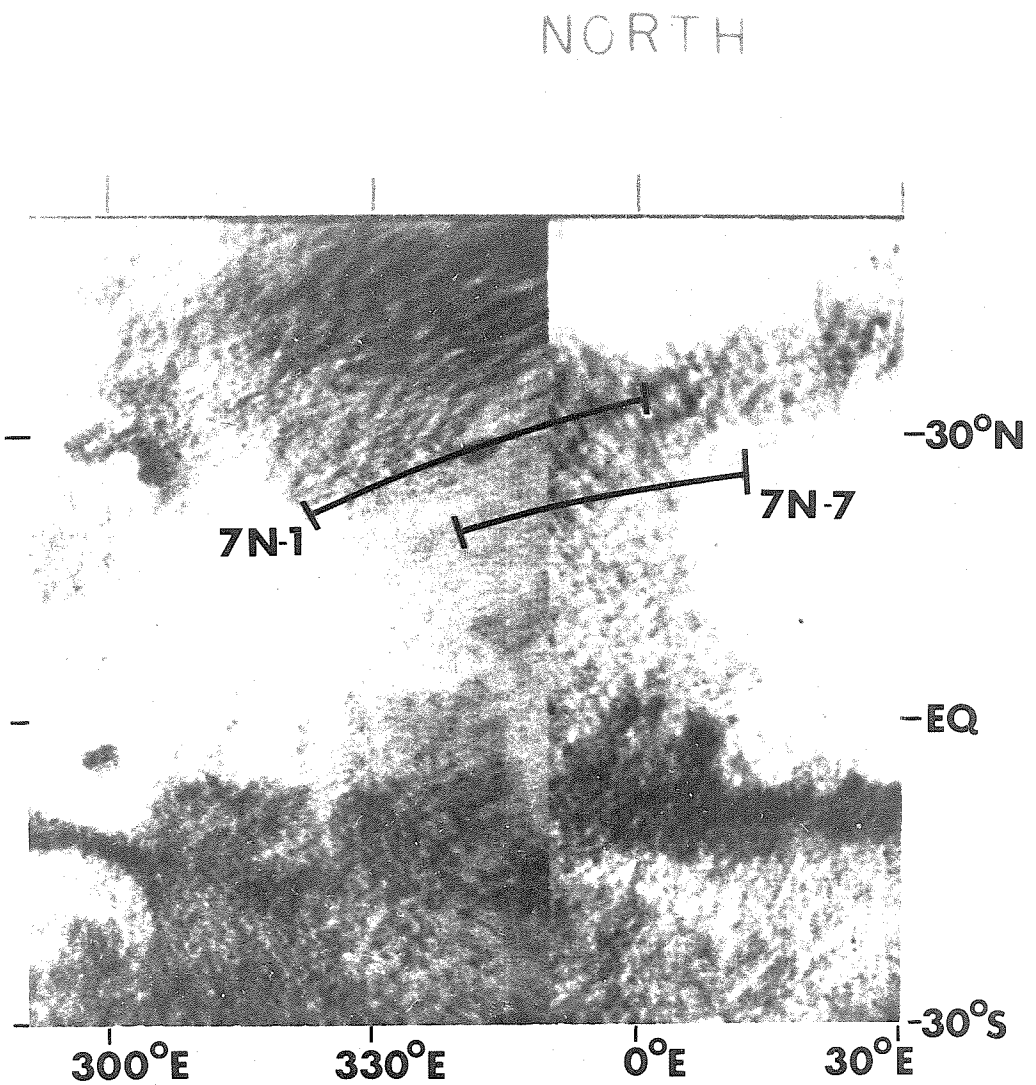

19. MOSAIC OF MERCATOR PROJECTIONS OF 7F67 AND 7F69

This shows the trace of the limb on the planet for frames 7N1 and 7 N7 of the previous figure. The haze layers identified in these frames appear as bright features in Moab and Chryse.

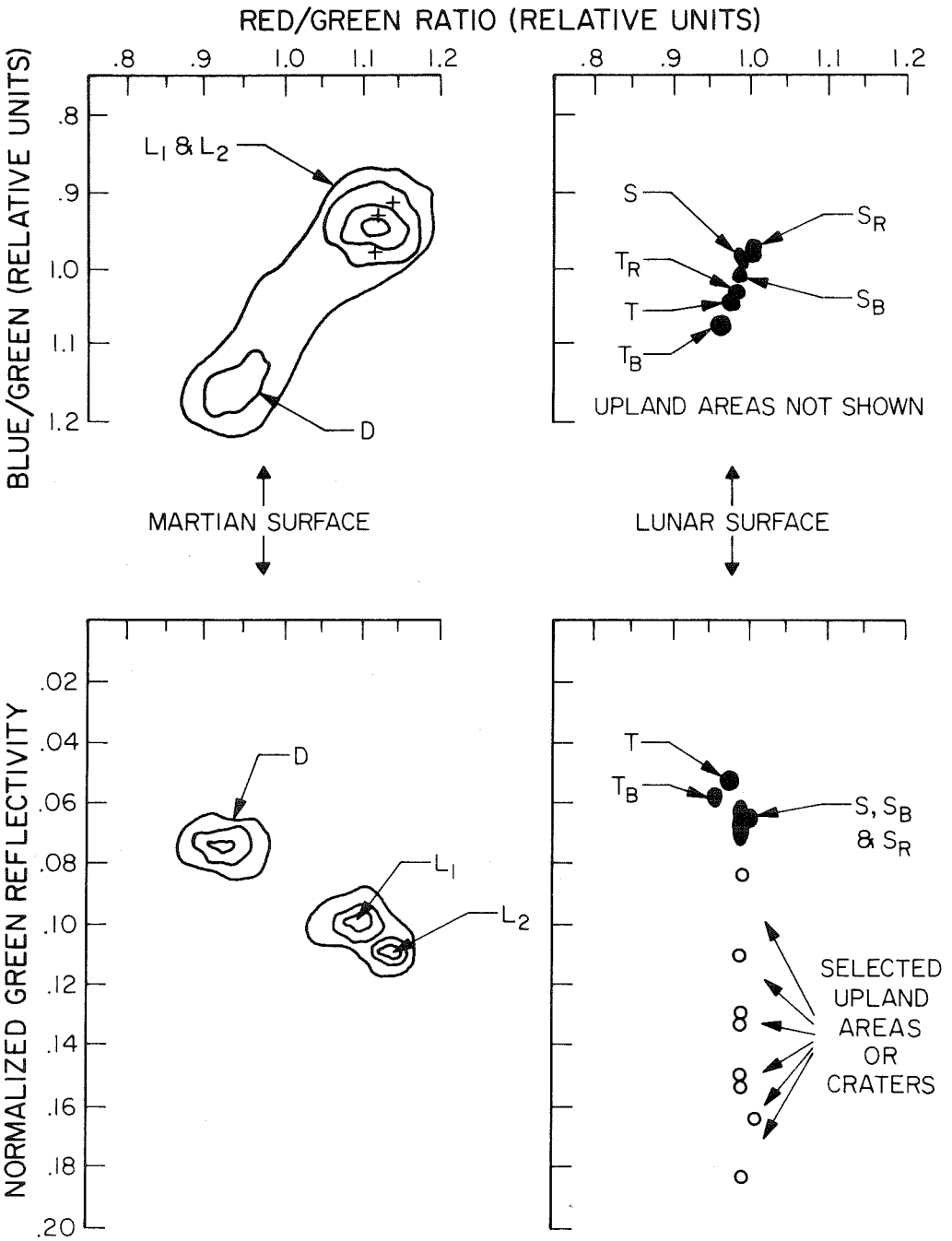

20. COMPARISON OF THE COLOR AND NORMAL ALBEDO DIFFERENCES ON THE LUNAR SURFACE WITH THOSE ON THE MARTIAN SURFACE

The color groups identified for the lunar surface are those proposed by Soderblom 1970.

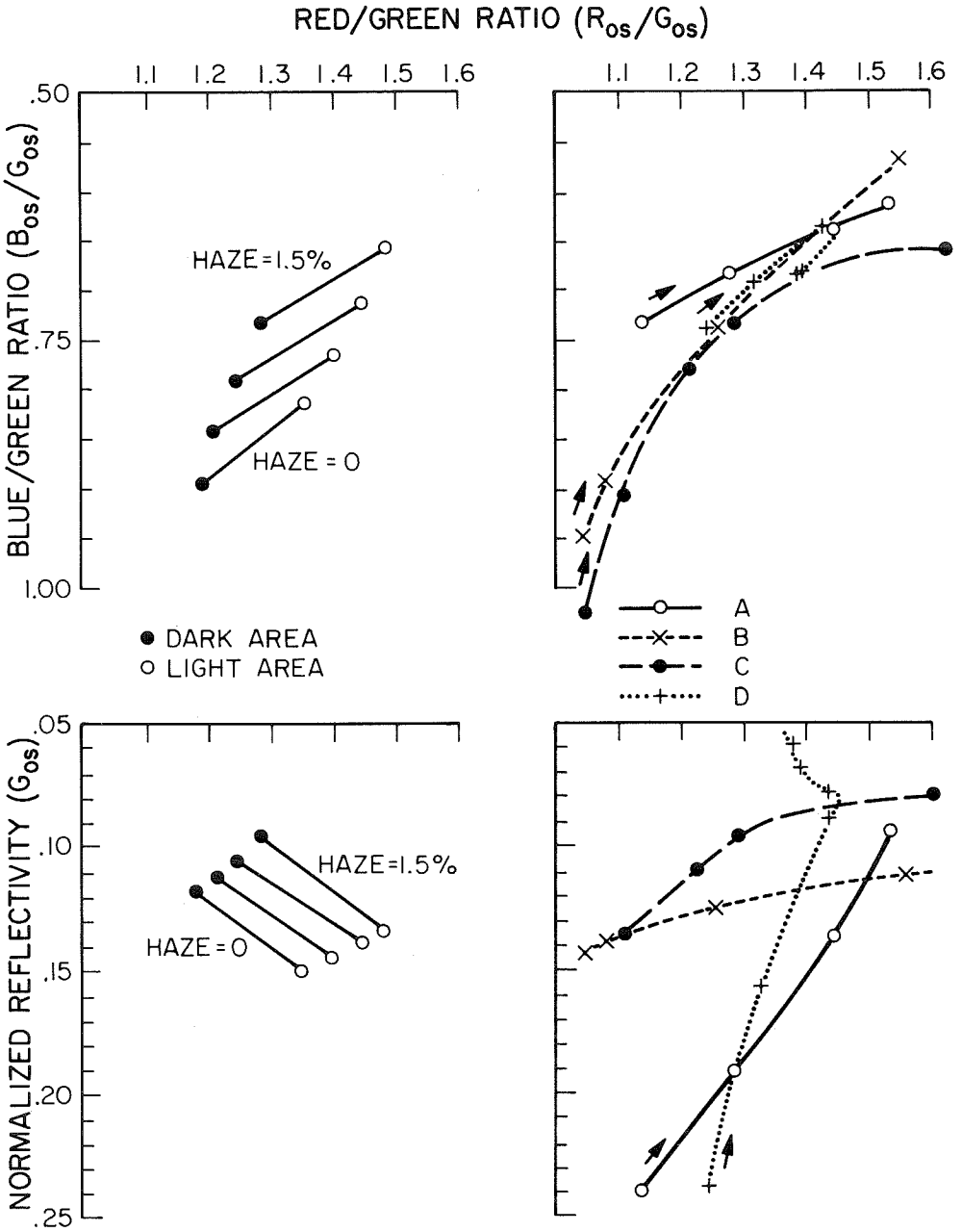

21. COMPARISON OF THE COLOR AND NORMAL ALBEDO DIFFERENCES ON MARS WITH THOSE FOR POSSIBLE SURFACE MATERIALS

Relative values of color and reflectivity of martian light and dark areas are insensitive to the presence of a uniform haze. A comparison is made with carbon suboxide (A) where the arrows show the effect of increasing polymerization and basalt where the arrows show successive additions of Goelhite (B), increasing oxidation state (C) and increasing particle size (D).

APPENDICES

APPENDIX A

THE NATURE OF THE MARINER 7 DIGITAL TELEVISION DATA AND ITS DECALIBRATION

1. INTRODUCTION

The Mariner 1969 television system was designed to maximize the number of high resolution high contrast pictures returned from Mars. Its complexity results from the conflict between this desire for a large amount of data and the technological limitations on storage and rate of transmission. The television system design is discussed in various amounts of detail by Leighton et al (1969) and Danielson et al (1971). Only the features pertinent to this paper are discussed here.

The television data compression system which minimized the amount of data needed to represent a high quality image of Mars, required the data leaving the vidicon image tube in the television to be divided into three data streams. Each stream was separately processed, stored and transmitted. The three data streams were recombined at the ground station as a first step to obtaining high resolution photometric (LMICOR) pictures.

Of the three data streams, analog, digital-every-seventh pixel (DV7) and digital-every-twenty-eight pixel (DV28), the first named, a high resolution non-photometric form, has been used in the photointerpretation work as maximum-discriminability pictures. It was not anticipated that there would be any independent application for DV7 or DV28 data. However, improvements in the technology of data transmission and reception made it possible to acquire, at one phase of the planetary encounter, DV7 data for full disc images of Mars taken through color filters. It was pointed out by

this author that this kind of data, although incomplete, could provide information about the spectral reflectivity of Mars of greater scientific value than could be obtained from earth or during other phases of the Mariner '69 mission. Following the success of Mariner 6, Mariner 7 was reprogrammed to acquire DV7 images.

1.a. DV7 data All three Mariner data streams are derived from the same vidicon television tube and consists of the digitally coded responses from a net of points on the surface of the sensor. The basic net consists of 945 samples equally spaced horizontally on 704 separate lines forming a total of 656,000 resolution elements or pixels. DV7 data (Fig.A(1a) are only transmitted for every seventh sample position. Moreover, telemetry from other science instruments uses the DV7 channel corresponding to the center of the frame resulting in a black data bar corresponding to the central 26 pixels of each DV line (Fig. A(1a). Therefore of 134 (= 945/7) possible DV samples per line, only 107 are transmitted.

Each DV7 sample was originally digitized to 8 bits (256 gray levels). However, only the six least significant bits (LSB's) were transmitted as part of the data compression scheme. The transfer function between the six bit data received on earth and the eight bit data encoded at the camera is indicated in Fig.A1b.

2. DECALIBRATION OF RAW TELEVISION DATA

For this study of the spectral reflectivity of Mars, two dimensional images characterising accurately the broad band reflectivity of the planet are required. The operations and techniques that were used to produce such images from the raw data received by the ground station are described

below. This process of decalibration was performed by the author using the programming system VICAR (Video Image Conversion and Retrieval system) and the facilities of the JPL Image Processing Laboratory (IPL).

2.a. Restoration of most significant bits Converting the raw six bit data as received by the ground station into an image (Fig. A2 (A→B) illustrates the contouring effect of removing most significant bits from image data. An algorithm devised by IPL engineers recognizes these contour lines and hence deconvolves the transfer curve of Fig. A1(b) giving an image B bearing some resemblance to the original scene.

2.b. Removal of coherent noise Owing to a design deficiency, electronic pick up noise was introduced into the vidicon signal resulting in the basket weave effect in the image B of Fig. A2. Some success in reducing the amplitude of this coherent noise was achieved by averaging up to ten pictures taken through the same filters but this method was not adequately accurate for photometric analysis. It was necessary therefore to remove the noise by Fourier Transform Methods.

Techniques for removing coherent noise in images had been developed by the IPL staff (Rindfleish et al 1971). However, the noise in DV7 pictures is at a much lower frequency relative to the sampling rate than in the analog pictures and was much more difficult to remove. The problem was compounded by the fact that the amplitude frequency and phase of the parasitic noise was not known from pre-flight calibration data but had to be identified in the actual images of Mars.

A successful method for removing coherent noise was arrived at after investigating several different approaches. The steps involved in

the successful method are illustrated in Fig. A2 (B→I).

The picture was first prepared for noise removal by removing sharp large amplitude changes in brightness. Such step functions generate high frequencies and aggravate the problem of separating image frequencies from parasitic coherent noise. Using the program NORING this was achieved in a completely reversible fashion. The noisy picture was split into two components a smooth version without sharp transitions (C) and its complement (D). It could be regenerated in its original form (B) by subtracting D from C.

The spatial frequency components of C were obtained using a two dimensional Fourier transforms (FFT2). Several harmonic series of frequency spikes can be recognized in the Fourier transform (E). After several trial and error operations, those spikes corresponding to the parasitic frequencies were separated from the frequencies making up the noise-free image using a mask for filter (F) and then reconstituted by an inverse transform into a noise pattern (G). The noise amplitude in the smoothed picture (C) was determined by trial subtractions and the optimal noise removal was achieved using the criterion of minimum variance. The resultant image H was reconstituted into a noise free image (I) by subtraction of the complement picture (D).

2.c. Reseau removal geometric correction and residual removal Vidicon reseaus were recognized in the pictures and were replaced by linear interpolation from surrounding picture elements. This reduced the occurrence of reflectivity and color artifacts in the subsequent analysis. Using preflight calibration data and various cross checks, corrections for electronic and

optical geometric distortion were applied and the residual signal from the previous frame was removed from each image.

2.d. Photometric correction In order to determine characteristics of the spectral composition of the light entering the camera from the signals delivered by the vidicon a point by point application of the television camera light transfer characteristics has been made (Danielson et al 1971). The original data number at each picture element is replaced by the broad band reflectivity, which can then be more explicitly connected with the spectral reflectivity of the martian surface and atmosphere.

$$R = \text{Broad band reflectivity} = \frac{\int^{\lambda} V_\lambda \, F_\lambda \, S_\lambda \, R_\lambda \, d_\lambda}{\int V_\lambda \, F_\lambda \, S_\lambda \, d_\lambda}$$

V_λ = Relative vidicon spectral response

F_λ = Relative filter spectral transmission

S_λ = Relative solar spectrum

R_λ = Absolute spectral reflectance of Mars

A lambert surface at the distance that Mars was from the sun at Mariner encounter (1.428 A.U.) would have absolute reflectivity $R_\lambda = 1$ and a broad band reflectivity $R = 1$ through all filters. It is not possible to determine in detail the spectral curve of Mars from broad band reflectivity measurements through red, green and blue filters. One can, however, determine its general shape or confirm

detailed spectral reflectivity curves obtained by ground based observers. For the purpose of making computations using 8 bit numbers the broad band reflectivity units were converted to IPL reflectance units (IPLRU's).

IPL Reflectivity (IPLRU's) = 1200 x Broad band reflectivity

Plots of F_2 and V_2 for the Mariner 7 wide angle camera are given in Fig. A3. The broad band reflectivities R, B, G, and G_2 were calculated for Martian light and dark areas using values of S_λ given by Allen (1962) and values of R_λ given by McCord (1969). The integrals were evaluated by Simpson's Rule using integrands evaluated every 5 microns. The comparison with the Mariner 7 measurements is made in the text.

3. PHOTOMETRIC PRECISION

Calibration of the Mariner television system has been discussed by Danielson and Montgomery (1971) and the accuracy of the resulting decalibrated data by Rindfleisch et al (1971). There are photometric errors in the decalibrated data due to changes in the responsivity of the camera between launch and planetary encounter, but their extent is extremely difficult to assess. The photometric errors do not, however, substantially affect the conclusions presented in the text because these conclusions are based primarily on relative photometry. Relative photometry is much less sensitive to responsivity changes than absolute photometry.

Errors in the color ratio measurements do occur because of the every-seventh-element sampling. This is most evident where there are rapid changes in reflectivity and color such as within the dark area Meridiani Sinus. These errors are discussed in the text.

APPENDIX B

MERCATOR PROJECTIONS

Conversion of the photometric images of Mars to a Mercator projection for the purpose of registration and the detailed comparison with other data referred to this projection was a two step process. The first step was a cartographic problem - to relate the coordinates of line and sample number (x,y) (Fig. A1 (a)) to the areocentric coordinates of latitude (Φ) and longitude (λ) on the surface of the planet.[1]

a. Cartography

Data on the trajectory and orientation of the spacecraft permitted the calculation of Φ_{ss}, λ_{ss} the latitude and longitude of the subspacecraft point and N, the angle between the projection of the planetary axis and the television scan lines (Campbell, 1970). The Polar radius of the planet in pixel units (picture element units) was also measured from the photometric images. This data were sufficient to construct latitude and longitude grid lines at the scale of each image in the right orientation but it was still necessary to find some means of registering the grid to the image.

The most obvious method of registration is with the limb of the planet. This is not possible because the limb is truncated in the late far

[1] No information was available on the third areocentric coordinate radius (R) and it was assumed to be constant.

encounter pictures (Fig. B1). The terminator of the planet is visible and its theoretical trace for a spherical airless planet can be computed from the latitude and longitude of the subsolar point (Φsz, λsz). If there is an atmospheric haze above the surface as appears to be the case for Mars the actual terminator does not correspond to the theoretical trace. A 20 km high haze displaces the terminator approximately 200 km from its theoretical value. Since the height of the Martian haze is variable and uncertain the terminator is not useful for registration of the latitude-longitude grid.

A method was developed by the author using small well defined albedo features which were visible in the far-encounter (FE) and near-encounter (NE) as well as these LFE pictures. The image plane coordinates (x_r, y_r) were determined for these features in the LFE picture and their latitude and longitude ($_r$, λ_r) determined in near-encounter picture 7N5 for which an accurate latitude-longitude grid had been developed by Davies and Berg (1971). The location of the subspacecraft point (Φ_{ss}, λ_{ss}) in the image plane (x_{ss}, y_{ss}) was then determined using the methods of spherical trigonometry (Fig. B1)

$$x_{ss} = x_r + R \sin c \cos (b + N) \quad (1)$$

$$y_{ss} = y_r + R \sin c \sin (b + N) \quad (2)$$

where

$$\cos c = \sin \Phi_{ss} \sin \Phi_r + \cos \Phi_{ss} \cos \Phi_r \cos (\lambda_{ss} - \lambda_r) \quad (3)$$

$$\cos b = (\sin \Phi_r - \sin \Phi_{ss} \cos c) / \cos \Phi_{ss} \sin c \quad (4)$$

After calculating x_{ss} and y_{ss} for three different x_r,y_r and

determining the mean value equations (1) and (2) were manipulated in order to calculate (x, y) for 10° increments of λ and Φ over the range of 300°E to 50°E longitude and $+30^{\circ}$N to -40°S latitude.

b. The Projection

The important element in making the actual Mercator projection is an image processing program called GEOM. GEOM takes a quadrelateral section as an input image and transforms it into a rectangle in the output image. Clearly, if the quadrilateral in the input follows the trace of intersecting latitude and longitude lines (Fig. B2), then the output image can be programmed to approximate a Mercator projection. In order to apply GEOM to the task of making Mercator sections, it is necessary to know the location in pixel coordinates (x, y) of the corners of the quadrilaterals determined by the latitude and longitude lines in the original image.

These points were evaluated from equations (1), (2), (3), (4) above at 10° intervals. A mercator projection of the region of the planet between 310°E and 40°E and 20°N and -35°S was generated (Fig. B2).

A Mercator projection of the same part of the planet was also made from a far-encounter (FE) picture. This was referred to the highly accurate cartographic control net of Davies and Berg (1971) and was used to check the Mercator projections for the LFE pictures by the methods discussed in the main part of the text.

APPENDIX C

MARTIAN PHOTOMETRY

The reflectivity of a feature on the martian disc depends on three factors: (1) wavelength, (2) the three angular coordinates required to describe the illumination and viewing geometry (local geometry) and (3) the nature of light scattering by the martian surface and atmosphere. The Mariner 7 photometric data consist of partial images of the disc in which the local geometry varies from feature to feature. In order to interpret the wavelength dependence of reflectivity in terms of the atmospheric and surface properties it is therefore necessary to evaluate the effect of local geometry and to reduce the measurements to standard conditions.

1. The empirical photometric function for martian bright areas

The dependence of brightness on viewing and illumination geometry is expressed by a photometric function. An analytic expression which seems to fit the measured brightness (P) of Mars for the rather limited local geometrics that it has been observed under is the Minnaert law. (Young 1969).

This has the form

$$P(\alpha, i, \varepsilon, \lambda) = P(\alpha,\lambda)\,(\cos i)^{k(\alpha,\lambda)}\,(\cos \varepsilon)^{k(\alpha,\lambda)-1} \qquad (1)$$

where α = phase angle (See Fig. C1a)

i = angle of incidence

ϵ = angle of viewing

k = adjustable parameter

There is no physical basis for this function other than that it satisfies the reciprocity principle (Minnaert 1960).

A.T. Young (private comm.) finds the following values for K and α for the bright desert regions of Mars.

$$k\ (\alpha,\lambda) = 19/40 + 3/8\ \lambda + 1/100\ \alpha$$

$$P_o\ (\alpha,\lambda) = P_o\ (\lambda) + (4 \times 10^{-5} + 1.33 \times 10^{-4}\lambda) \cdot \alpha \cdot (\alpha - 2\alpha_o)$$

where $\alpha_o = \begin{cases} 40^\circ, & \lambda \leq 0.45\mu \\ 40^\circ - 70'(\lambda - 0.45), & \lambda > 0.45\mu \end{cases}$ (2)

The form of these functions has no particular physical significance since the functions are chosen to best conform with earth-based data on the photometric properties of the planet. The functions are very much simplified when they are applied to the Mariner images because the variation of phase angle across each image is small ($23 \pm 2^\circ$) and P (α) and R (α) are not strong functions of α in this range.

2. Photometric function of the martian surface

The photometric function discussed above applies to the total light reflected from these regions - that is from the atmosphere as well as the surface. However it assumes that the amount of light scattered by the atmosphere is small and consequently its range of validity does not extend to the limb where the amount of atmospheric light will be large. One would naturally adopt therefore the Minnaert function in essentially

the same form to model the light scattered from the surface alone.

$$\text{Surface reflectivity } \mathcal{R}_s = \mathcal{R}_{os}\ (\alpha, \lambda) \cos i \left[\frac{k_s(\alpha, \lambda)}{\cos \epsilon} - k_s(\alpha, \lambda) - 1 \right] \tag{3}$$

3. Photometric function of the martian atmosphere

In general, the photometric function of an atmosphere is dependent upon the highly complex solutions for radiative transfer within it. In the case of an optically thin atmosphere which is applicable to most of the equatorial areas of Mars then simple solutions are available. The reflectivity for an optically thin haze is given by the formula.

$$\text{Reflectivity } \mathcal{R}_a = \frac{\pi B}{F_o} = \left[1 - \exp(-M\tau) \right] \frac{P1(\alpha)}{4} \tag{4}$$

where B = Brightness of layer τ = normal optical depth

F = flux of incident radiation $P1(\alpha)$ = phase function

M = air mass α = phase angle

For regions far from the limb equation (4) has a similar form:

$$\mathcal{R}_a = M\tau \frac{P1(\alpha)}{4} = \sec \epsilon\ \tau \frac{P1(\alpha)}{4} \tag{5}$$

The general scattering law for particles is extremely complex. The Mie Theory (Vander Hulst 1957) provides an analytic solution for electromagnetic scattering on spherical particles of any given size. This has been extended to distributions of particle sizes (spherical polydispersions) by Deirmendjian (1969). Limiting cases of the Mie Theory

which are used to model the martian atmosphere are Rayleigh scattering and white or neutral scattering.

3.a. Rayleigh scattering

Particles very much smaller than the wavelength of light ($a < \lambda/10$) scatter light according to the Rayleigh law for which

$$\tau = \tau_o \frac{\lambda_o^4}{\lambda^4} \qquad (6)$$

$$P1(\alpha) = 3/4 \ (1 + \cos^2 \alpha) \qquad (7)$$

τ_o can be expressed in terms of the size, number, density, refractive index and polarizing properties of the particle.

3.b. Neutral (white) scattering

For non absorbing particles very much larger than the wavelength of light ($a > 10 \lambda$) the scattering cross section is independent of wavelength and

$$\tau = \tau_o \qquad (8)$$

The phase law P1 (α) is sensitive to the particle size distribution and wavelength but displays strong forward scattering.

4. Photometric function of surface and atmosphere

On the planet Mars, light is scattered in the atmosphere and at the surface. Neglecting multiple scattering between the atmosphere and ground which will be small if the haze is optically thin since the surface reflectivity is low then the total reflectivity (R_t) observed by the

television camera is

$$\mathcal{R}_t = \mathcal{R}_a + \mathcal{R}_s \quad . \qquad (9)$$

where $\mathcal{R}_a$ and $\mathcal{R}_s$ are specified in equations (3) and (4) above.

5. Application of the photometric formulae

The empirical photometric function (1) is used in the comparison of the Mariner 7 measurements of broadband reflectivity with the earth based measurements presented in the review paper by McCord et al. This is described in section 3.

The photometric functions for the surface and atmosphere appearing in equations (3) and (5) are applied in the analysis of the Mariner 7 photometric data of section 5. These functions are evaluated at each point in the image using values of cos i and cos ε calculated from an orthographic approximation (Fig. C1(b)).

$$\cos i = \cos \Phi_{sz} \cos \Phi \cos (\lambda - \lambda_{sz}) + \sin \Phi_{sz} \sin \Phi \qquad (10)$$

$$\cos \epsilon = \cos \Phi_{ss} \cos \Phi \cos (\lambda - \lambda_{ss}) + \sin \Phi_{ss} \sin \Phi \qquad (11)$$

$(\Phi_{sz}, \lambda_{sz})$ are the coordinates of the subsolar point.

The trigonometric functions in equations (3) and (4) are generated as arrays in the Mercator geometry so that simple additive and multiplicative operations can be performed directly on the photometric data.

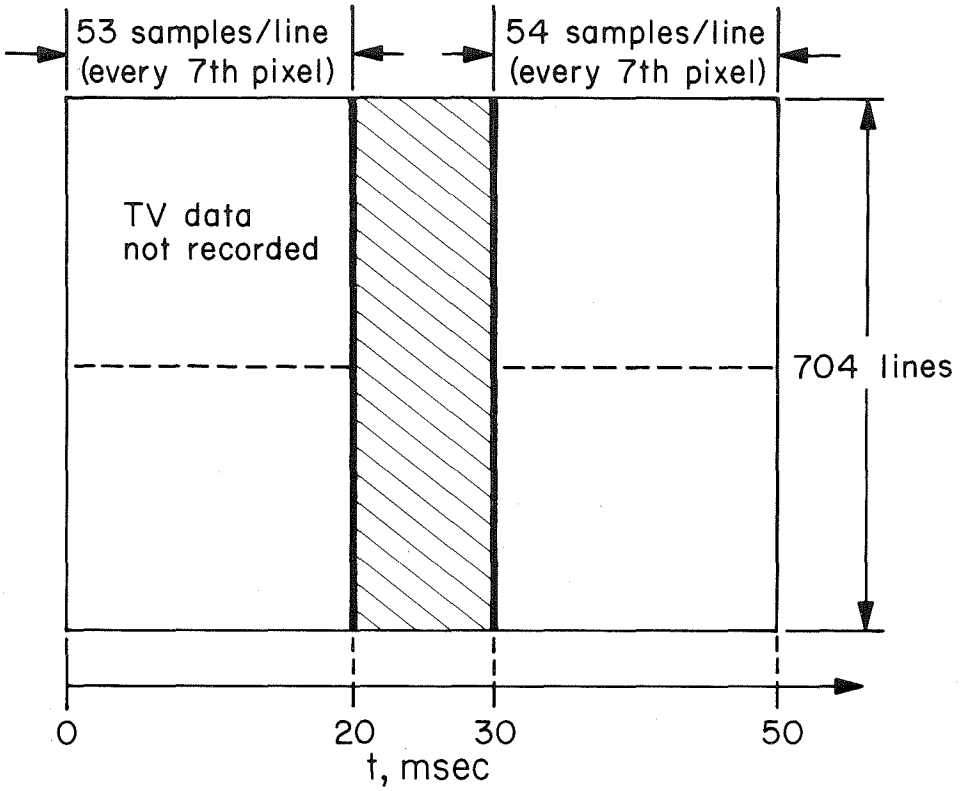

A1 (a) DIGITAL VIDEO (DV7) FORMAT

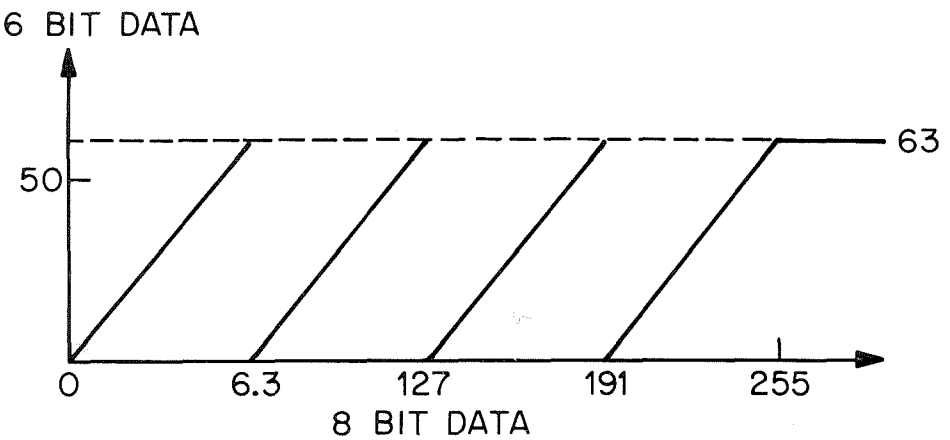

(b) TRANSFER FUNCTION BETWEEN ORIGINAL 8-BIT DV7 AND THE SIX-BIT DATA

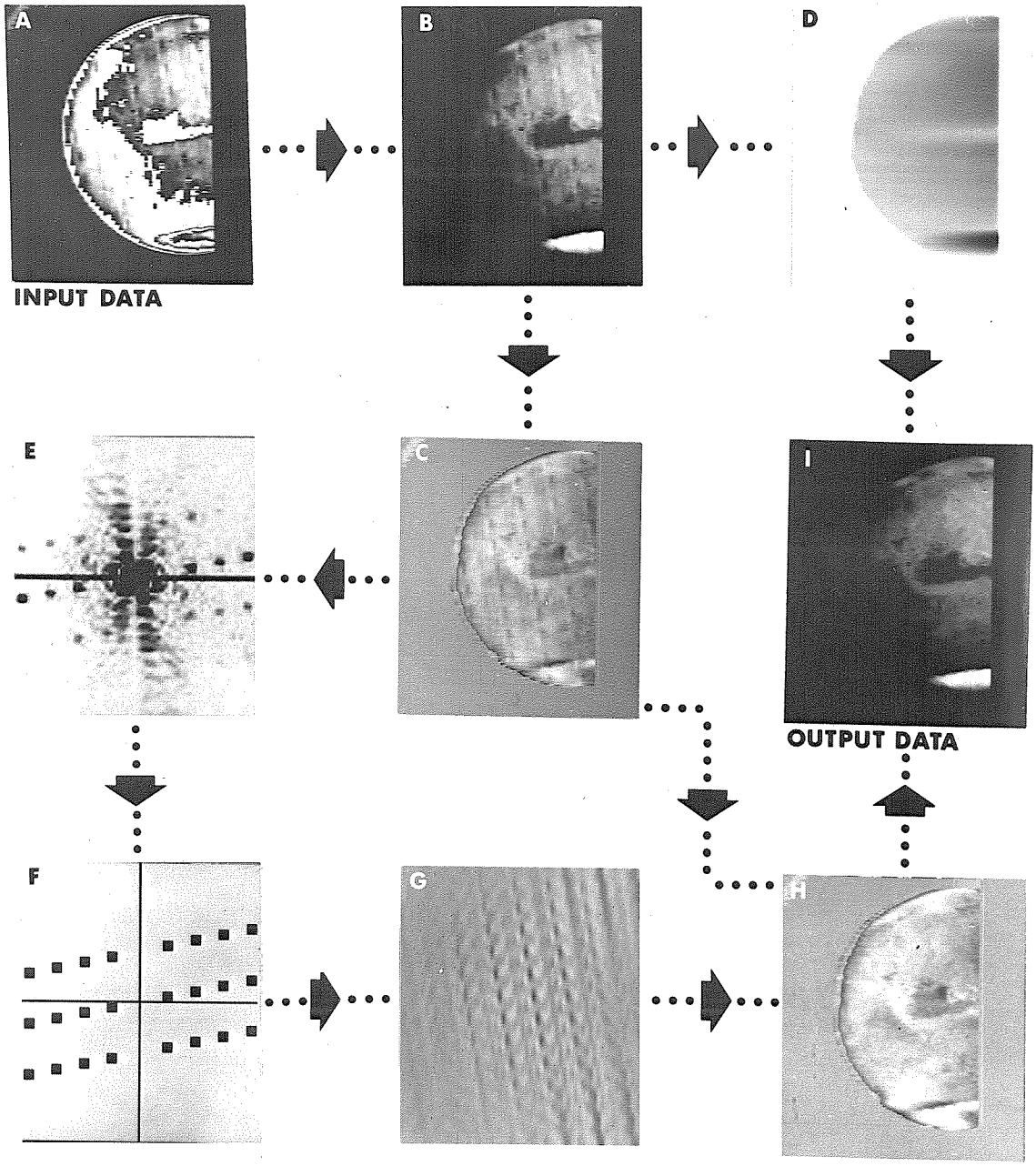

A2 THE REMOVAL OF COHERENT NOISE FROM PHOTOMETRIC DATA

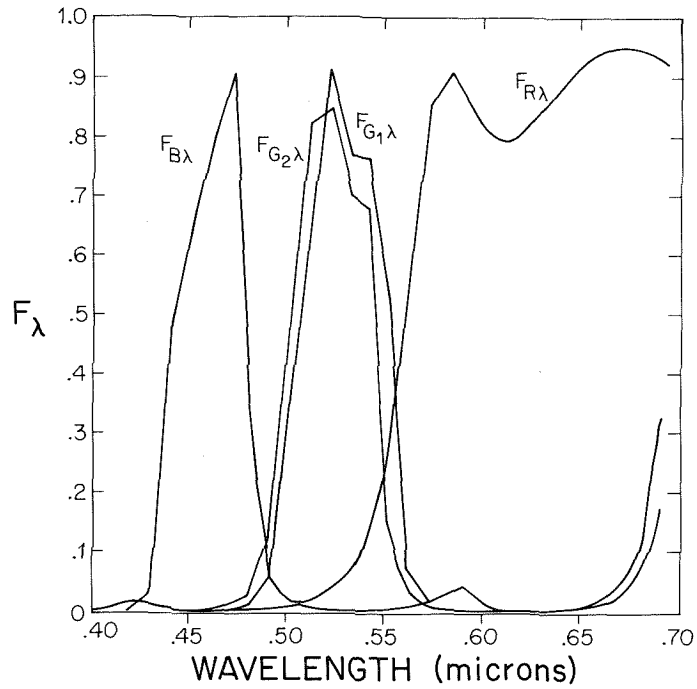

A3 (a) SPECTRAL TRANSMISSION OF MARINER 7 COLOR FILTERS

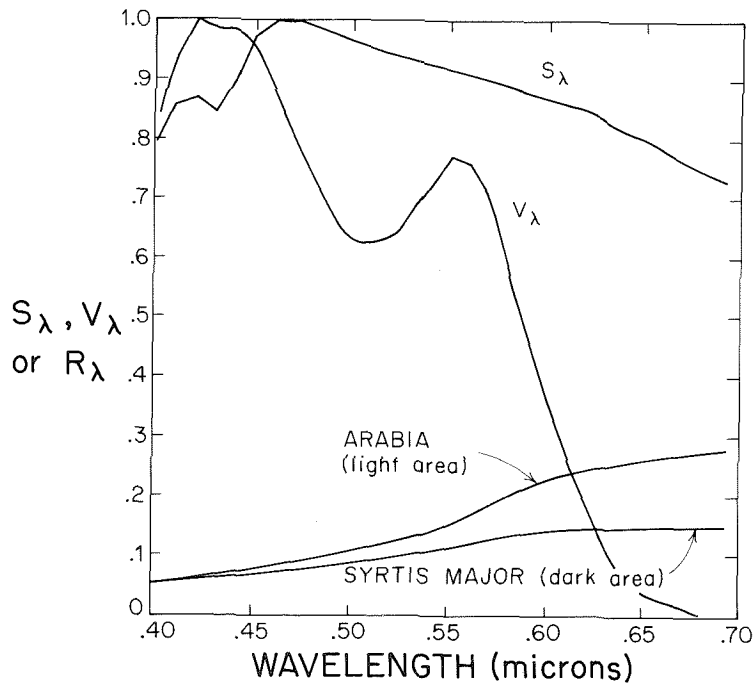

A3 (b) SOLAR SPECTRUM AND VIDICON RESPONSE, SPECTRAL REFLECTIVITY OF LIGHT AND DARK AREAS OF MARS (EARTH-BASED MEASUREMENTS)

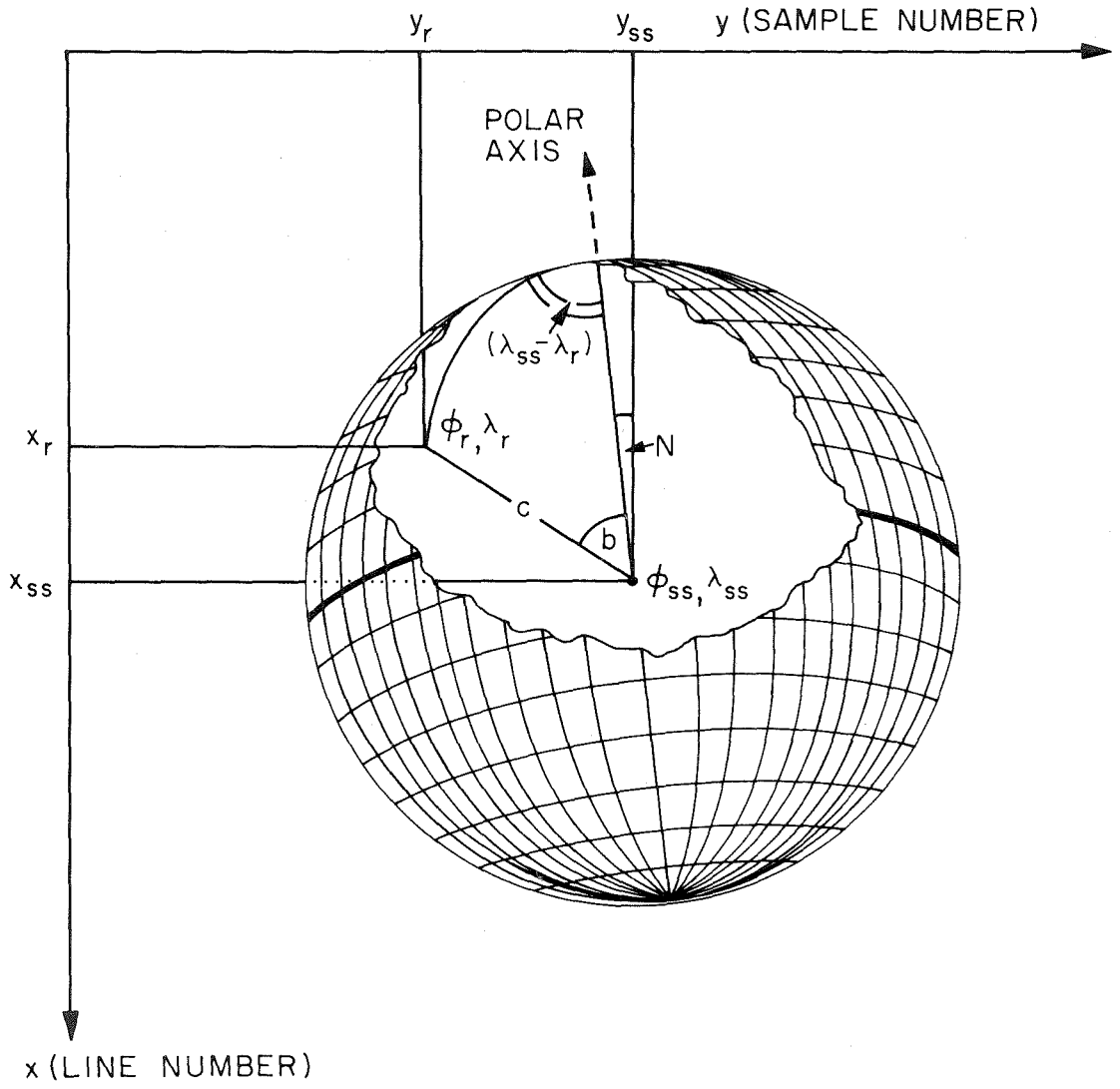

B1 GEOMETRY OF IMAGES OF MARS

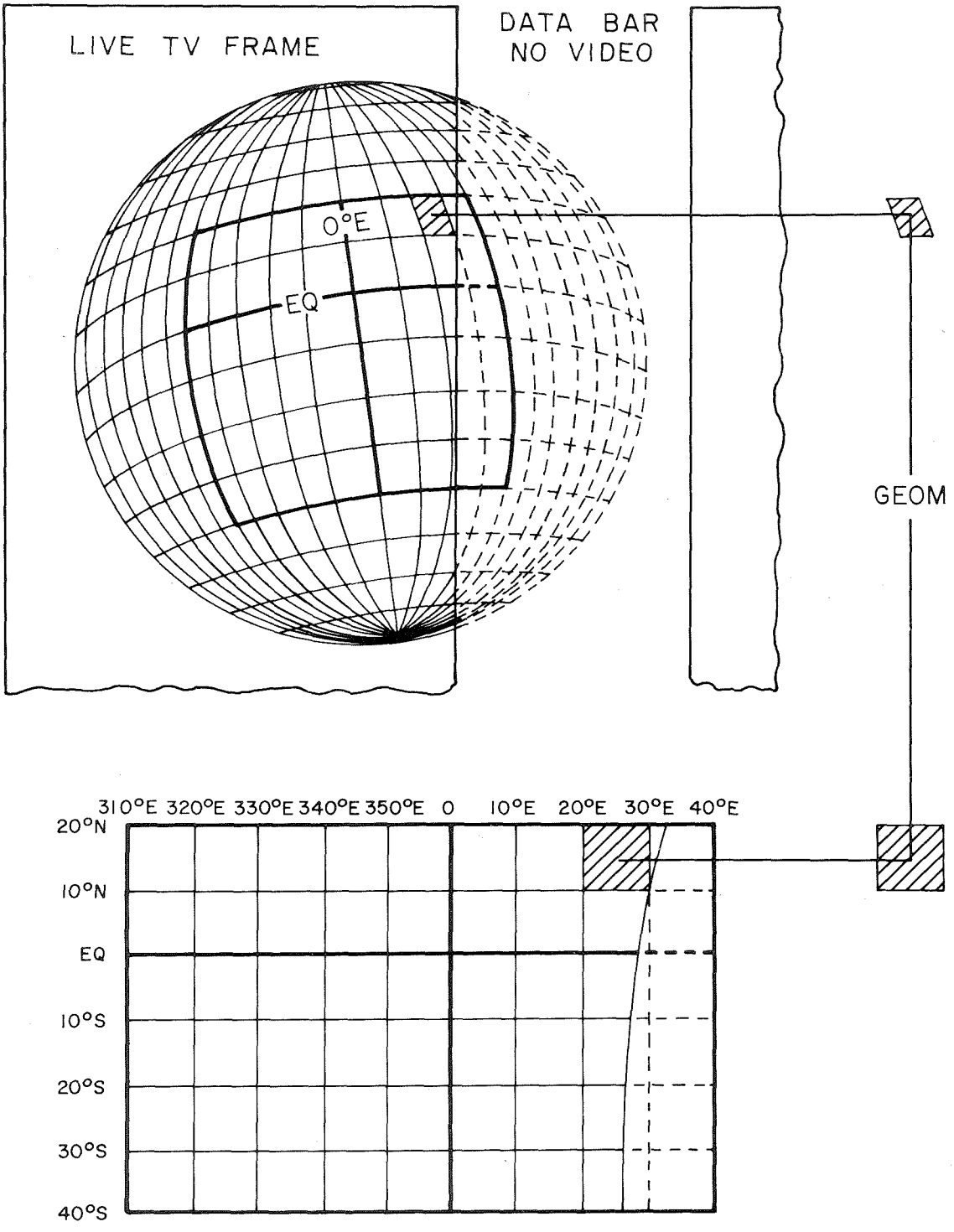

B2 FORMATION OF MERCATOR PROJECTIONS

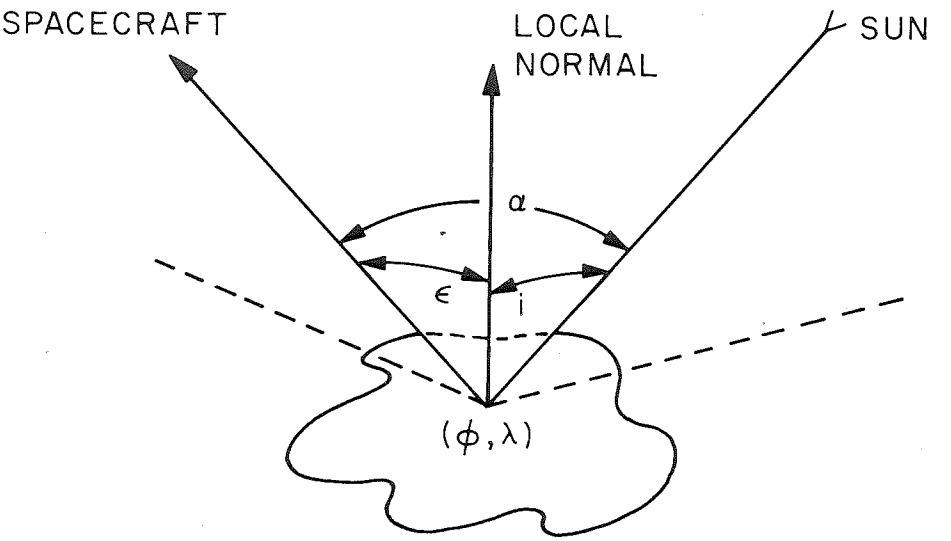

C1 (a) LOCAL GEOMETRY OF ILLUMINATION AND VIEWING

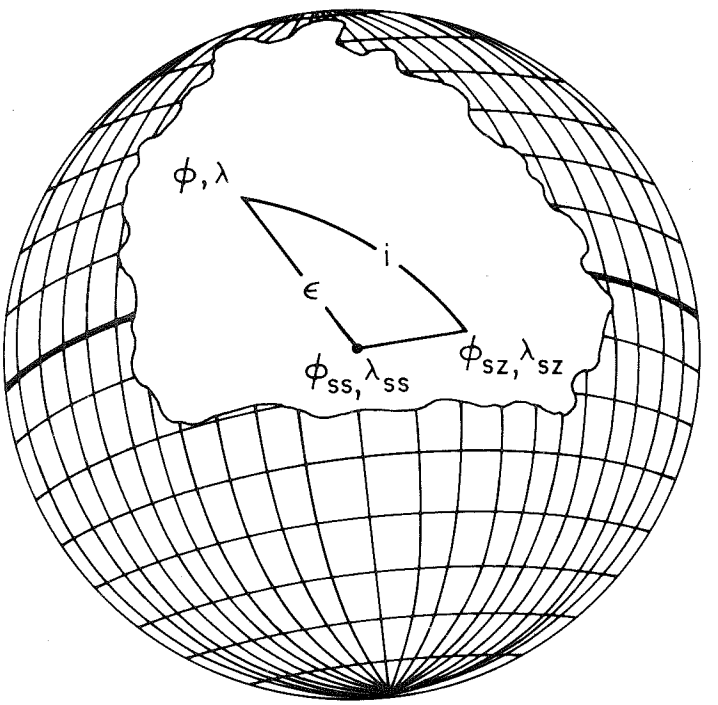

(b) ORTHOGRAPHIC APPROXIMATION FOR ANGLE OF INCIDENCE AND VIEWING ANGLE (ϵ)

REFERENCES

Adams, J.B., Lunar and Martian Surfaces: Petrological Significance of Absorption Bands in the Near-Infrared, Science, 159, 1453, 1968.

Adams, J.B., Spectral Reflectivity of Lunar Samples, Science, 167, 737, 1970.

Adams, J.B. and T.B. McCord, Mars: Interpretation of Spectral Reflectivity of Light and Dark regions, J. Geophys. Res. 74, No. 20, 4851-4856, 1969.

Albee, A.L., D.S. Burnett, A.A. Chodos, O.J. Eugster, J.C. Huneke, D.A. Papanastassiov, F.A. Podosek, G. Price Russ II, H.G. Sanz, F. Tera and G.J. Wasserberg, Ages, Irradiation History and Chemical Composition of Lunar Rocks from the Sea of Tranquility, Science, 167, 463, 1970.

Allen, C.W. Astrophysical Quantities, 291 pp., The Athlone Press, University of London, 1962.

Campbell, J.K., Mariner Mars 1969 Simulated Television Pictures (Final), JPL Document 605-237, 1970.

Cutts, J.A., L.A. Soderblom, R.P. Sharp, B.A. Smith and B.C. Murray, The surface of Mars III - Light and dark markings, J. Geophys. Res., 76, No. 2, pp._____, January 10, 1971a.

Cutts, J.A., G.E. Danielson and M.E. Davies, A mercator photomap of Mars, J. Geophys. Res., 76, No. 2, pp._____, January 10, 1971b.

Davies, M.E., and R.A. Berg, A Preliminary control net for Mars, J. Geophys. Res., 76, No. 2, pp._____, January 10, 1971.

Danielson, G.E. and D.T. Montgomery, Calibration of the Mariner Mars 1969 Television cameras, J. Geophys. Res., 76, No. 2, pp._____ January 10, 1971.

Deirmendjian, D., Electromagnetic scattering on Spherical Polydispersions, 290pp., American Elsevier Publishing Co., New York, 1969.

Dollfus, A., Contribution au Colloque Caltech-JPL sur la lune et les planetes: Mars, pp. 288-304 of Proceedings of the Caltech-JPL Lunar and Planetary Conference, September 13-18, 1965, JPL Technical Memorandum No. 33-266, 1966.

REFERENCES
(continued)

Herr, K.C., D. Horn, J M. McAfee and G.C. Pimental, Martian topography from Mariner 6 and 7 infrared spectra, Astronom. J., (in press).

Herr, K.C. and G.C. Pimental, Infrared absorption near three microns recorded over the polar cap of Mars, Science, 166, 496-499, 1969.

Hord, C.W. and C.A. Barth, Mariner 6 and 7 ultraviolet spectrometer results (submitted to Science), 1970.

Lunar Sample Preliminary Examination Team, "Preliminary Examination of Lunar Samples from Apollo 12, Science, 167, 1325, 1970.

Leighton, R.B., N.H. Horowitz, B.C. Murray, R.P. Sharp, A.H. Herriman, A.T. Young, B.A. Smith, M.E. Davies, and C.B. Leovy, Mariner 6 and 7 television pictures: Preliminary analysis, Science, 166, 49-67, 1969.

Leovy, C.B., B.A. Smith, A.T. Young and R.B. Leighton, Mariner Mars '69: Atmospheric Results, J. Geophys. Res., 76, No. 2, pp._____, January 10, 1971.

McCord, T.B., Color Differences on the Lunar Surface, Ph.D. Dissertation, California Institute of Technology, Pasadena, 1968.

McCord, T.B. and J.B. Adams, Spectral reflectivity of Mars, Science 166 1058-1060, 1969.

Minnaert, M., Photometry of the Moon, Chapter 6 of Planets and Satellites, G.P. Kuiper, ed., University of Chicago Press, 1961.

Murray, B.C., L.A. Soderblom, R.P. Sharp and J.A. Cutts, The surface of Mars: I - Cratered terrains, J. Geophys. Res., 76, No. 2, pp._____, January 10, 1971.

Plummer, H.T. and R.K. Carson, Mars: Is the surface colored by Carbon Suboxide?, Science, 166, 1141-1142, 1969.

Rea, D.C., The darkening wave on Mars, Nature, 201, 1014-1015, 1964.

Rindfleisch, T.C., J.A. Dunne, H. Frieden, W.D. Stromberg, R. Ruiz, Image processing of the Mariner 6 and 7 pictures, J. Geophys. Res., 76, No. 2, pp._____, 1971.

Sagan, C. and J.B. Pollack, Windblown dust on Mars, Nature, 223, 791-794, 1969.

Salisbury, J.W., and G.R. Hunt, Martian Surface Materials: Effect of Particle Size on Spectral Behavior, Science, 161, 365-366, 1968.

REFERENCES
(continued)

Sharp, R.P., L.A. Soderblom, B.C. Murray and J.A. Cutts, The surface of Mars: II - Uncratered terrains, J. Geophys. Res., 76, No. 2, pp._____, January 10, 1971.

Slipher, E.C., The Photographic Story of Mars, 168pp., Sky Publish. Co., Cambridge, Mass., 1962.

Soderblom, L.A., The Distribution and Ages of Regional Lithologies in the Lunar Maria, Ph.D. Dissertation, California Institute of Technology, 1970.

Van de Hulst, H.C., Light scattering by Small Particles, 470 pp., John Wiley & Sons, New York and London, 1957.

Van Tassel, R.A., and J.W. Salisbury, The composition of the martian surface, Icarus, 3, 264-269, 1964.

Young, A.T., High-Resolution Photometry of a Thin Planetary Atmosphere, Icarus, II, 1, 1969.

Young, A.T., and S.A. Collins, The photometric properties of the Mariner cameras and of selected regions on Mars, J. Geophys. Res., 76, No. 2, pp._____, January 10, 1971.